

Loss-of-function mutations in *Dnmt3a* and *Tet2* lead to accelerated atherosclerosis and concordant macrophage phenotypes

Received: 6 October 2021

Accepted: 27 July 2023

Published online: 4 September 2023

 Check for updates

Philipp J. Rauch  , Jayakrishnan Gopakumar  , Alexander J. Silver , Daniel Nachun³, Herra Ahmad , Marie McConkey^{1,2}, Tetsushi Nakao  , Marc Bosse , Thiago Rentz⁶, Nora Vivanco Gonzalez³, Noah F. Greenwald , Erin F. McCaffrey³, Zumana Khair³, Manu Gopakumar⁷, Kameron B. Rodrigues , Amy E. Lin^{1,2,6}, Eti Sinha , Maia Fefer⁶, Drew N. Cohen¹, Amélie Vromman⁶, Eugenia Shvartz⁶, Galina Sukhova⁶, Sean Bendall³, Michael Angelo , Peter Libby , Benjamin L. Ebert  & Siddhartha Jaiswal  

Clonal hematopoiesis of indeterminate potential (CHIP) is defined by the presence of a cancer-associated somatic mutation in white blood cells in the absence of overt hematological malignancy. It arises most commonly from loss-of-function mutations in the epigenetic regulators *DNMT3A* and *TET2*. CHIP predisposes to both hematological malignancies and atherosclerotic cardiovascular disease in humans. Here we demonstrate that loss of *Dnmt3a* in myeloid cells increased murine atherosclerosis to a similar degree as previously seen with loss of *Tet2*. Loss of *Dnmt3a* enhanced inflammation in macrophages *in vitro* and generated a distinct adventitial macrophage population *in vivo* which merges a resident macrophage profile with an inflammatory cytokine signature. These changes surprisingly phenocopy the effect of loss of *Tet2*. Our results identify a common pathway promoting heightened innate immune cell activation with loss of either gene, providing a biological basis for the excess atherosclerotic disease burden in carriers of these two most prevalent CHIP mutations.

Clonal hematopoiesis of indeterminate potential (CHIP) is defined by the presence of specific somatic mutations with a variant allele fraction of $\geq 2\%$ in the blood or bone marrow of individuals who do not fulfill other diagnostic criteria for a hematological malignancy^{1,2}. CHIP associates strongly with aging, with between 10% and 20% of those over the

age of 70 harboring a mutant clone. We previously found that CHIP is associated with an $\sim 40\%$ increase in all-cause mortality, which appeared to be primarily due to an increased risk of atherosclerotic cardiovascular disease, the leading cause of death globally³. In fact, the presence of a CHIP clone, in particular one with a variant allele fraction $\geq 10\%$,

¹Department of Medical Oncology, Dana-Farber Cancer Institute, Boston, MA, USA. ²Broad Institute of Harvard and MIT, Cambridge, MA, USA.

³Department of Pathology, Stanford University School of Medicine, Stanford, CA, USA. ⁴Division of Hematology, Department of Medicine, Brigham and Women's Hospital, Boston, MA, USA. ⁵Cardiovascular Research Center and Center for Genomic Medicine, Massachusetts General Hospital, Boston, MA, USA. ⁶Cardiovascular Division, Department of Medicine, Brigham and Women's Hospital, Boston, MA, USA. ⁷Department of Electrical Engineering, Stanford University, Stanford, CA, USA. ⁸Howard Hughes Medical Institute, Boston, MA, USA. ⁹Institute for Stem Cell Biology and Regenerative Medicine, Stanford University School of Medicine, Stanford, CA, USA. ¹⁰These authors contributed equally: Philipp J. Rauch, Jayakrishnan Gopakumar.

 e-mail: philipp_rauch@dfci.harvard.edu; sjaiswal@stanford.edu

conferred a fully adjusted greater risk of atherosclerotic disease than most traditional risk factors, such as smoking status, obesity, blood pressure and cholesterol levels, in a recent study².

The most commonly mutated gene in CHIP, *DNMT3A*, encodes a de novo DNA methyltransferase that catalyzes the production of 5-methylcytosine, a well-characterized transcriptional regulator^{4,5}. The second most commonly mutated gene, *TET2*, encodes an enzyme that sequentially oxidizes 5-methylcytosine, initiating the demethylation process^{6,7}. Surprisingly, despite their opposing biochemical functions, mutations in either gene lead to convergent phenotypes, such as clonal expansion of mutated stem cells^{8,9}, increased risk of malignant transformation^{10,11}, myeloid differentiation bias¹² and increased risk of coronary heart disease, based on epidemiological data¹³. A protective polymorphism in the *L6R* gene also attenuates the risk of atherosclerotic cardiovascular disease in those with either gene mutated¹⁴. Mutations in *TET2* or *DNMT3A* also worsen heart failure in nonatherosclerotic mice and lead to increased mortality in patients with heart failure^{15,16}.

A molecular mechanism linking CHIP and atherosclerosis has been explored for loss-of-function mutations in the *Tet2* gene, involving overexpression of proinflammatory chemokines and cytokines and activation of the NLRP3 inflammasome^{13,17}. In the present study, we explored the effect of *Dnmt3a* loss on the development of atherosclerosis in mice, revealing several proinflammatory changes in macrophages that may predispose to lesional progression.

Results

Loss of *Dnmt3a* function in myeloid cells accelerates atherosclerosis

To investigate the association between *Dnmt3a* loss of function and atherosclerosis, we transplanted bone marrow from mice lacking *Dnmt3a* in hematopoietic cells (knockout (KO): *Dnmt3a*^{fl/fl}; *Vav1-Cre*) or control mice (wild-type (WT): *Dnmt3a*^{+/+}; *Vav1-Cre*) into irradiated, atherosclerosis-prone *Ldlr*^{-/-} mice. The recipient *Ldlr*^{-/-} mice received bone marrow either at a 1:9 KO:WT ratio to mimic a typical clone size observed in humans with *DNMT3A* and *TET2* loss-of-function mutations² or from WT cells as a control. These mice were placed on an atherogenic diet after allowing time for hematopoietic reconstitution from donor marrow. At 9 weeks after initiation of the high-fat, high-cholesterol diet, mice transplanted with 10% KO bone marrow had ~40% larger aortic root lesions compared with mice transplanted with only WT marrow (Extended Data Fig. 1a,b). This increase in lesion size is modestly lower than what we and others previously observed in *Ldlr*^{-/-} mice receiving *Tet2*^{-/-} marrow^{13,17}. As expected, the mutant cell fraction had expanded preferentially in the myeloid compartment, representing, on average, 38% of myeloid cells in the peripheral blood at that timepoint (Extended Data Fig. 2a). Of note, mice transplanted with heterozygous *Dnmt3a*^{+/-} bone marrow did not display increased lesion size at 9 weeks, in contrast to previous experiments with *Tet2*^{-/-} bone marrow where haploinsufficiency led to a significant increase in lesion size¹³ (Extended Data Fig. 1c). Of note, when we examined lesion size in the root in advanced atherosclerosis (20 weeks on the diet), there was no significant difference between the groups (Extended Data Fig. 1d,e), similar to what we previously reported with loss of *Tet2*.

As infiltrating monocytes and macrophages are key cellular protagonists that initiate and drive atherosclerosis^{18,19}, we asked whether loss of *Dnmt3a* limited to myeloid cells sufficed to yield increased atherosclerosis in this system. To generate mice with myeloid-specific deletion of *Dnmt3a*, animals expressing Cre recombinase under the *Lyz2* promoter were crossed with mice bearing floxed alleles of *Dnmt3a*. Bone marrow from the resulting *Dnmt3a*^{fl/fl}; *Lyz2-Cre* mice was transplanted into irradiated *Ldlr*^{-/-} mice. Compared with mice that received only WT bone marrow, these mice had, on average, 46% larger aortic root lesions (Fig. 1a,b), indicating that *Dnmt3a* loss in cells of the myeloid lineage suffices to accelerate atherosclerosis. When we examined lesional composition, we found an increase in macrophage content

and a decrease in collagen cap content in mice that had received KO marrow compared with WT controls (Fig. 1c–e).

As previous studies have suggested a proportional relationship between monocytosis and atherosclerotic plaque burden²⁰, we profiled peripheral blood cell counts over time. Mice receiving bone marrow from KO mice had normal levels of peripheral white blood cells, a normal hematocrit and a normal platelet count during the study period, consistent with observations in humans with *DNMT3A*-mutant CHIP¹³. Furthermore, blood differential cell counts including the absolute monocyte count did not differ when comparing mice that received KO marrow and controls at 8 weeks on a high-cholesterol diet, although there was a modest increase in platelet count and absolute monocyte count in recipients of KO marrow at 20 weeks on the diet (Extended Data Fig. 2b). Lipids being key to atherogenesis, we further profiled total, high-density lipoprotein- and low-density lipoprotein- (LDL)-cholesterol as well as triglycerides in the serum after 14 weeks on the diet. There was no significant difference between KO and WT groups in any of the measured lipids (Extended Data Fig. 2c), indicating that the acceleration of atherosclerosis in animals with *Dnmt3a*-deficient marrow is not likely to have been mediated by changes in systemic lipid metabolism.

Macrophages lacking *Dnmt3a* or *Tet2* have a concordant proinflammatory and atherogenic phenotype in vitro

Because of the key roles of *Dnmt3a* and *Tet2* in regulating DNA methylation and transcription, we asked whether loss of either gene modulated gene expression in the specific context of atherosclerosis. We previously demonstrated that bone marrow-derived macrophages (BMDMs) that lacked functional *Tet2* stimulated with LDL particles expressed significantly higher levels of proinflammatory chemokines and cytokines compared with WT BMDMs¹³. In the present study, we tested the transcriptional response of *Dnmt3a*^{-/-} BMDMs exposed to LDL particles and contrasted the results to *Tet2*^{-/-} BMDMs. Unbiased gene set enrichment analysis (GSEA) of Kyoto Encyclopedia of Genes and Genomes (KEGG) pathways showed that the most highly enriched pathways for both *Dnmt3a*- and *Tet2*-deficient macrophages, when compared with WT, were implicated in inflammation (Fig. 2a); a significant proportion of enriched pathways overlapped between the genotypes, even though additional pathways were dysregulated in the context of *Dnmt3a* loss (Extended Data Fig. 3a,b and Supplementary Table 1). Among the most highly enriched processes were cytokine–cytokine receptor interaction, tumor necrosis factor (TNF) signaling, interleukin (IL)-17 signaling and atherosclerosis-related pathways (Fig. 2a and Extended Data Fig. 3a). At the level of individual genes, BMDMs lacking functional *Dnmt3a* showed significantly increased expression of chemokines, cytokines, inflammatory response genes and cell-surface receptors after stimulation compared with WT BMDMs (Fig. 2b, Extended Data Fig. 4a and Supplementary Table 2). Many transcripts that were increased in *Dnmt3a*^{-/-} BMDMs relative to WT BMDMs were shared with those increased in *Tet2*^{-/-} BMDMs after similar stimulation (Extended Data Fig. 4b), and included *Cxcl1*, *Cxcl2*, *Cxcl3*, *Il1b*, *Il6*, *Saa3*, *Fpr1* and *Cd38*. As IL-1β, in particular, is emerging as a central mediator of increased inflammation in CHIP in humans²¹, we validated its increase in both *Dnmt3a*- and *Tet2*-mutant BMDMs at the protein level using intracellular flow cytometry (Extended Data Fig. 4c). ELISA further demonstrated increased secretion of CXCL1, CXCL2, CXCL3 and IL-6 from LDL-stimulated *Dnmt3a* KO BMDMs (Extended Data Fig. 4d), as was previously shown for *Tet2* (ref. 13).

To demonstrate formally a concordance of transcriptional profiles for both mutants, we used two complementary approaches. First, we analyzed the distribution of the most enriched and depleted transcripts from *Dnmt3a*^{-/-} BMDMs ($\log_2(\text{fold-change}) (\log_2(\text{FC})) > 0.5, P < 0.05$) in *Tet2*^{-/-} BMDMs. Under the null hypothesis, we would expect up- and downregulated genes in *Dnmt3a*^{-/-} BMDMs to be randomly up- or downregulated in *Tet2*^{-/-} BMDMs. The distributions for both permutations

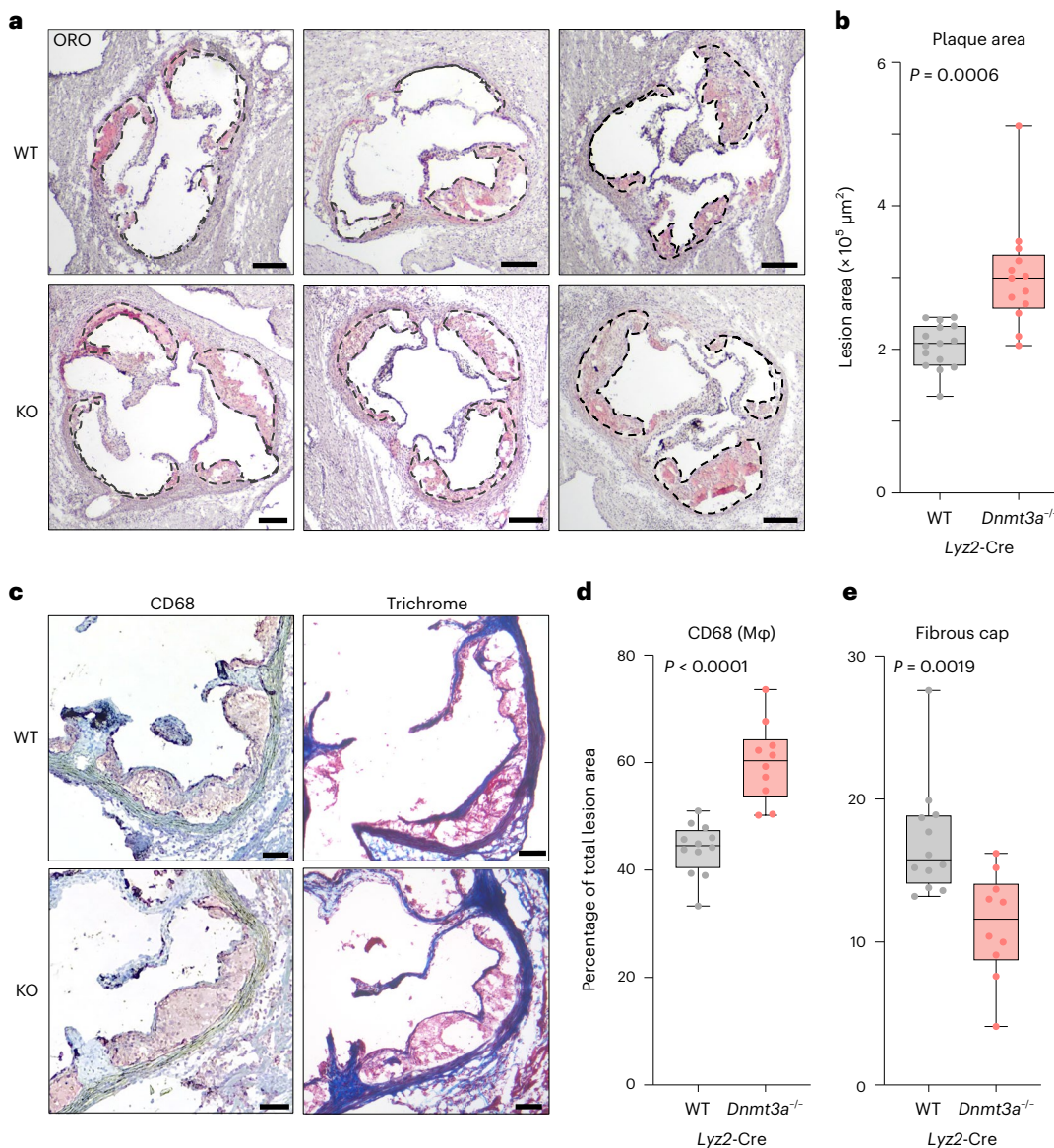


Fig. 1 | Loss of *Dnmt3a* function in myeloid cells accelerates atherosclerosis and increases lesional macrophage content. **a**, ORO-stained aortic root sections in female *Ldlr*^{-/-} mice transplanted with either *Dnmt3a*^{+/+};Lyz2-Cre (WT) or *Dnmt3a*^{-/-};Lyz2-Cre (KO) marrow after 8 weeks of feeding on a high-fat, high-cholesterol diet. Atheromata are demarcated by dashed lines. Scale bars, 200 μm . **b**, Quantification of lesion area in the aortic root in the cohort depicted in **a** ($n = 15$ animals for WT and $n = 13$ for KO group). An unpaired, two-tailed Student's *t*-test with Welsh's correction was used. The box plot shows minimum, 25th percentile, median, 75th percentile and maximum. **c**, IHC for CD68 and Masson's Trichrome stain on aortic root sections in the Lyz2-Cre cohort

in *Tet2*^{-/-} approximated the original distributions in *Dnmt3a*^{-/-} and differed significantly from a random distribution as assessed by the χ^2 test (Fig. 2c). To evaluate the specificity of this approach, we performed the same test in BMDMs with mutated *Jak2* known to cause inflammation in macrophages and accelerate atherosclerosis via a distinct mechanism²²; indeed, we did not find significant concordance with *Jak2*-mutated macrophages (Extended Data Fig. 3c). Second, we generated a gene set comprising the group of transcripts with highest differential expression in *Tet2*^{-/-} BMDMs ('*Tet2* KO pathway') and found a strong and statistically highly significant enrichment in *Dnmt3a*^{-/-} BMDMs (normalized enrichment score (NES) = 2.52, $P = 2.7 \times 10^{-12}$) (Fig. 2d).

The immune cell composition and transcriptional landscape of atheromata in vivo is altered by the loss of *Dnmt3a* or *Tet2*
Atherosclerosis involves a complex interplay of a multitude of different hematopoietic cell types within the arterial wall²³. We wondered whether the loss of *Dnmt3a* or *Tet2* in hematopoietic cells affected plaque immune cell composition and gene expression in vivo. To this end, we transplanted *Ldlr*^{-/-} mice with a mix of 10% *Dnmt3a* or *Tet2* KO bone marrow from donor mice with a CD45.2 background and 90% WT bone marrow from donor mice with a CD45.1 background. Control *Ldlr*^{-/-} mice received only WT marrow. After 30 weeks on a high-cholesterol diet, we dissected and enzymatically digested the ascending aortas, arches and descending aortas, generating a single-cell

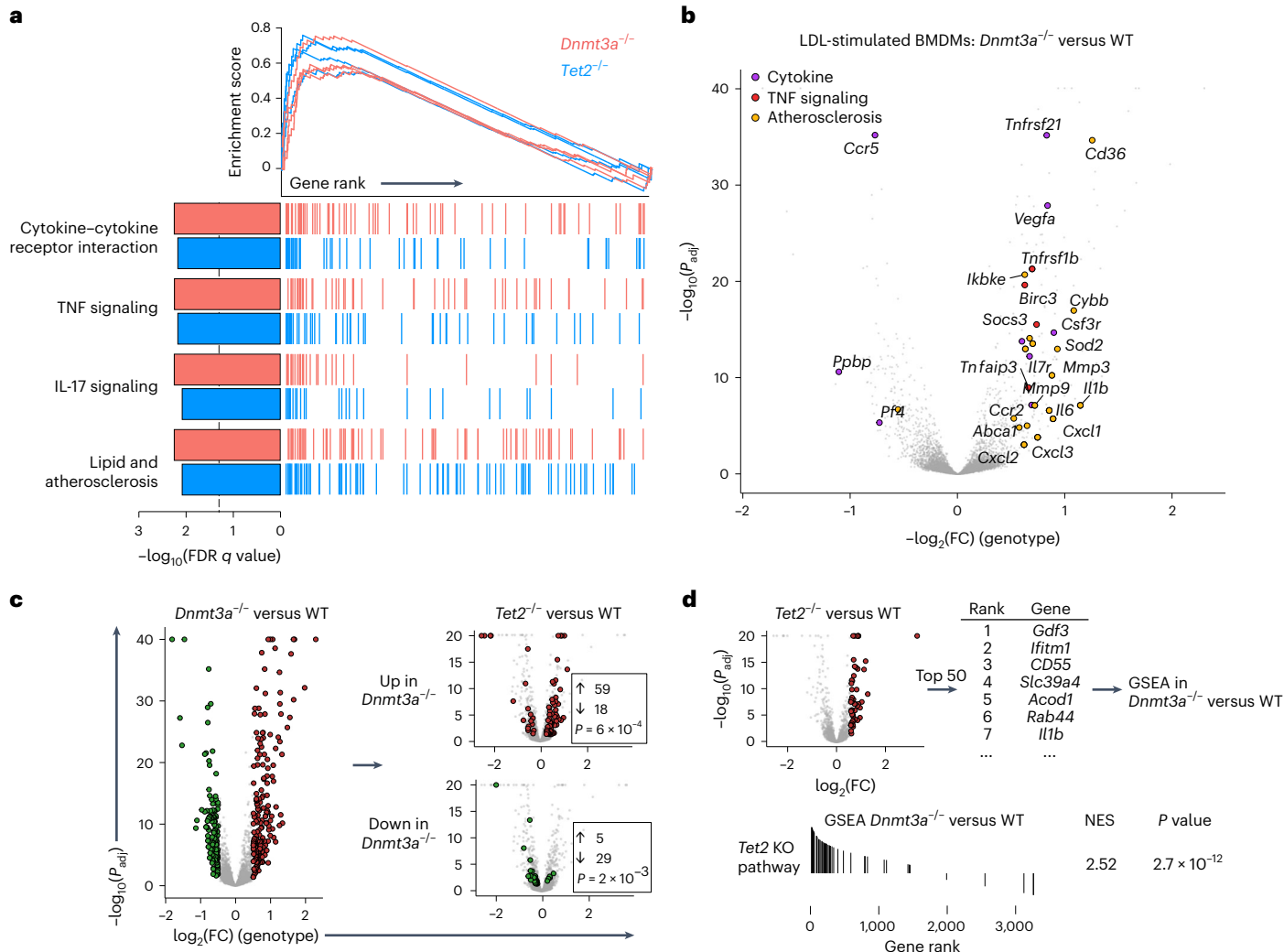


Fig. 2 | Loss of *Dnmt3a* and *Tet2* in BMDMs converge on to a proinflammatory and atherogenic phenotype. **a**, Mountain plots show cumulative enrichment of selected KEGG pathways involved in inflammation and aging in *Dnmt3a^{-/-}* versus WT BMDMs contrasted with *Tet2^{-/-}* versus WT, obtained by GSEA. To enable comparative analysis, gene lists were length matched by selecting the top 3,812 genes by *P* value for LDL treatment effect for each genotype (corresponding to $P < 0.05$ for *Dnmt3a^{-/-}*). The ticks below the line correspond to the gene ranks in the differential expression datasets. The dotted line under the bar graph indicates the FDR (false discovery rate) *q* value of 0.05. *Tet2^{-/-}* versus WT RNA-seq data were also used in ref. 13. **b**, Volcano plot showing differential gene expression analysis in *Dnmt3a^{-/-}* versus WT BMDMs based on messenger RNA-sequencing. Displayed are all genes with a baseMean > 256. Labeled are genes with significantly altered expression and a $\log_2(\text{FC}) > 0.6$ or < -0.6 in the enriched KEGG

pathways, cytokine–cytokine receptor interaction ('Cytokine'), TNF signaling and lipid and atherosclerosis ('Lipid'). Data are based on three biological replicates per genotype and stimulation condition. The *P* values were calculated using the default Wald's test in DESeq2. **c**, Enriched ($\log_2(\text{FC}) > 0.5$ and $P < 0.05$, red dots) or depleted ($\log_2(\text{FC}) < -0.5$ and $P < 0.05$, green dots) transcripts in *Dnmt3a^{-/-}* versus WT BMDMs tested for enrichment or depletion ($P < 0.05$) in *Tet2^{-/-}* BMDMs (all genes with *baseMean* > 1,000). The resulting distribution was tested for randomness by way of a two-sided χ^2 test. **d**, GSEA for the top 50 genes significantly increased by *Tet2^{-/-}* and LDL stimulation ('Tet2 KO pathway') in *Dnmt3a^{-/-}* versus WT BMDMs (LDL-responsive genes, *baseMean* > 256). The *P*-value estimation in the fgsea method is based on an adaptive, multi-level split, Monte Carlo scheme.

suspension. This timepoint was chosen because it provides a sufficient number of cells for analysis and because the aorta at 30 weeks contains predominantly cellular plaques resembling aortic root lesions at much earlier timepoints. Using antibodies specific for the CD45.1 and CD45.2 isoforms, we were able to distinguish and separate immune cells of a *Dnmt3a* or *Tet2* KO background from WT-derived progeny by FACS, which was followed by single-cell RNA-sequencing (scRNA-seq) (Fig. 3a and Extended Data Fig. 5a). Of note, our approach provided internal WT control populations sorted from the same mouse as their mutant competitors, which controls for potential biases introduced during tissue processing.

After application of quality-control (QC) filters, a total of 16,496 cells were included in the analysis, with a range of number of cells per

sample between 2,770 and 3,766. Unsupervised Seurat-based clustering analysis of an aggregate of all samples divided the lesional hematopoietic cell population into 18 subpopulations, representing 12 major cell types/states^{24,25} (Fig. 3b and Supplementary Data File 2). The identified clusters corresponded to all major myeloid and lymphoid cell types known to be present in atherosclerosis and agreed with the results of recent scRNA-seq-based studies of murine atherosclerosis^{26–28}. Within the myeloid cell fraction, we identified the previously described plaque populations of monocytes, dendritic cells, granulocytes and three macrophage clusters: inflammatory (lesional) macrophages, TREM2^{hi} macrophages and TR macrophages (Fig. 3b,c and Extended Data Fig. 5b).

Next, we asked whether the cellular composition shifted based on genotype. *Dnmt3a* or *Tet2* KO cells preferentially contributed to

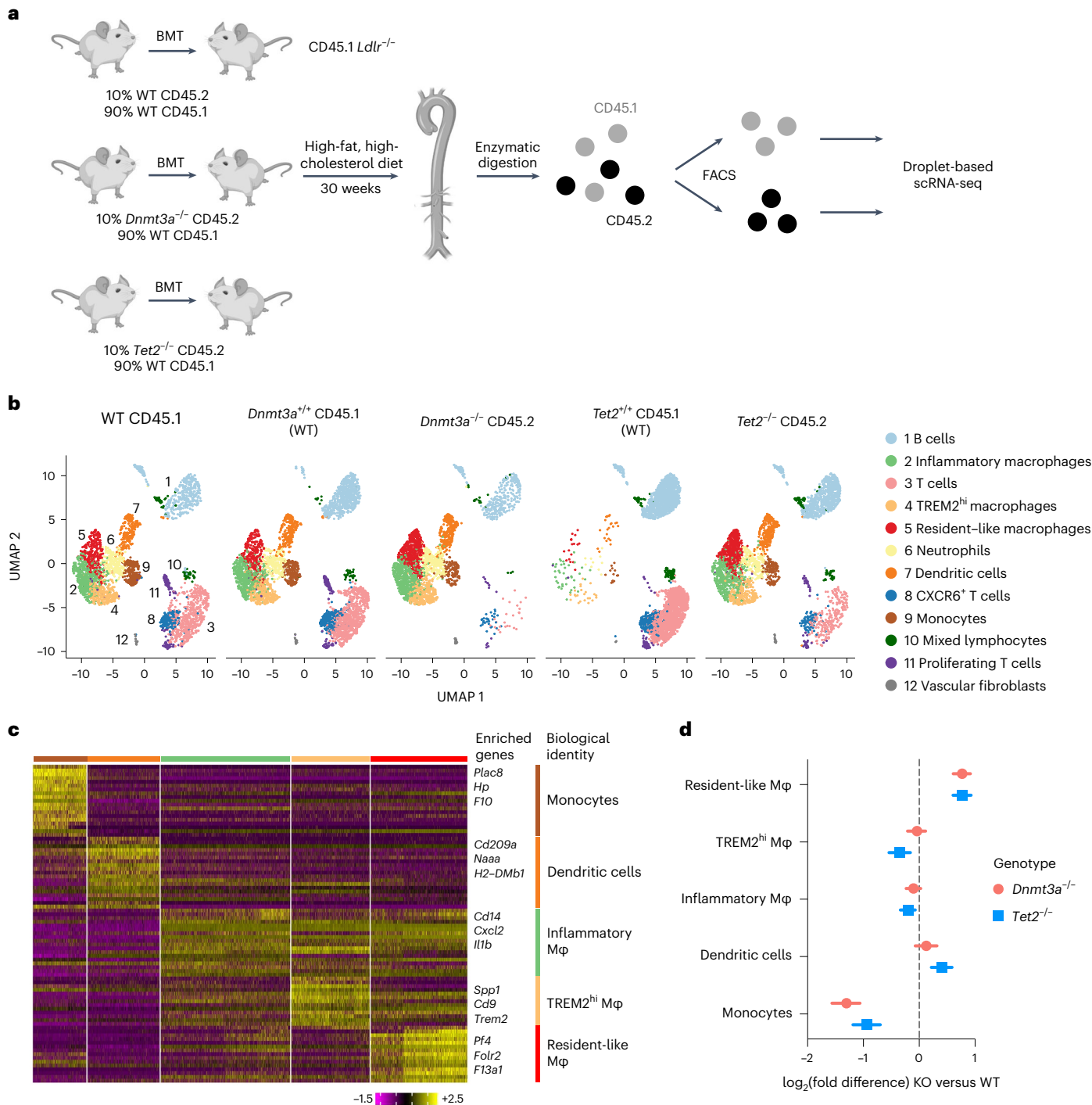


Fig. 3 | *Dnmt3a* and *Tet2* CHIP alter the immune cell composition in atheromata. **a**, Schematic diagram of the experimental design for scRNA-seq of atherosomata in bone marrow chimeric mice. Sorted samples represent pooled groups of three male mice per genotype. BMT, bone marrow transplantation. **b**, UMAP plots of aligned gene expression data in single cells isolated from aortae from WT; *Vav1-Cre* ($n = 3,230$), *Dnmt3a^{+/+};Vav1-Cre* ($n = 3,766$, competitively transplanted WT), *Dnmt3a^{-/-};Vav1-Cre* ($n = 2,770$), *Tet2^{+/+};Vav1-Cre* ($n = 3,540$, competitively transplanted WT) and *Tet2^{-/-};Vav1-Cre* ($n = 3,190$) populations. **c**, Heatmap of genes with increased expression in each mononuclear phagocyte

cluster compared with all other cell populations, across all samples. Displayed for each cluster are the top 20 genes with the highest average log(FC) present in at least 25% of the cells. Select enriched genes used for biological identification are listed (see Supplementary Data File 2 for an expanded list of signature genes).

d, Proportion-of-cluster analysis of the mononuclear subpopulations at 30 weeks, comparing *Dnmt3a^{-/-}* and *Tet2^{-/-}* with WT. Displayed is $\log_2(\text{fold difference})$ and 95% confidence interval. Permutation test with $n = 1,000$ permutations. Full statistics are reported in Supplementary Table 5.

the myeloid compartment and had reduced contribution to lesional lymphocytes, particularly in *Dnmt3a* KO (Fig. 3b and Extended Data Fig. 5c). The composition of the myeloid compartment also changed significantly in mutant cells, with a striking increase in the proportion

of TR macrophages (Fig. 3d and Supplementary Table 3). Within the monocytic compartment, we saw an expansion of Ly6C^{hi} classic monocytes, proinflammatory cells that have been demonstrated to preferentially traverse the endothelium and accumulate in atherosclerotic

plaques^{20,29} (Extended Data Fig. 5d). As local macrophage proliferation is known to contribute to atherosclerosis¹⁸, we also performed a transcriptome-based cell-cycle analysis on our scRNA-seq dataset. This analysis did not reveal relevant differences between WT and KO in any of the three major macrophage populations (Extended Data Fig. 5f), indicating that differences in proliferation are unlikely to be responsible for the increased lesional macrophage content seen in animals transplanted with mutant marrow.

A closer examination of the relative decrease of the lymphoid compartment showed that this was mainly attributable to a loss of CD8⁺ cytotoxic T lymphocytes, whereas B cells were relatively increased and CXCR6⁺ and proliferating T lymphocyte subsets showed little change (Extended Data Fig. 5e).

Atheromata with loss of hematopoietic *Dnmt3a* or *Tet2* harbor a distinct tissue resident-like macrophage population

Examination of the plaques' resident macrophage compartment revealed a distinct population among cells derived from mutant (CD45.2), but not WT (CD45.1), cells. The mutant resident-like macrophages expressed high levels of genes previously associated with WT aorta TR macrophages (*Mrc1* (encoding the surface marker CD206), *Lyve1*, *Folr2* and *F13a1*)^{27,28}, but also genes encoding several inflammatory and chemotactic mediators not highly expressed by WT tissue-resident macrophages (*Ccl8*, *Cxcl1*, *Ccl2* and *Ccl12*), as well as a characteristic set of early response transcription factor genes (*Jun*, *Fos* and *Egr1*) (Fig. 4a,b and Extended Data Fig. 6a).

Transcriptionally, these cells, which we named 'CHIP-tissue resident-like (TR) macrophages', resemble a composite profile of tissue-resident macrophages and activated/inflammatory macrophages. In addition, they bear markers unique to the cluster (Supplementary Table 4) and were far more prevalent in plaque cells of *Dnmt3a* or *Tet2* KO than of WT origin (Fig. 4c,d). Marked expansion of CHIP-TR macrophages was also seen by scRNA-seq in *Dnmt3a*- or *Tet2*-mutant plaque leukocytes in an independent cohort harvested at 24 weeks on the diet (Extended Data Fig. 7a,b; total of 29,206 cells analyzed across samples). Of note, these cells preferentially expanded between the 24- and 30-week timepoint in mutant populations, whereas their frequency remained stable in WT counterparts (Fig. 4d). The population's highly chemotactic and inflammatory signature implicates it as a putative cellular source of the chemokines that recruit myeloid cells to inflamed vessel walls. GSEA of the genes differentially increased within this cluster returned several pathways associated with inflammation and aging, highly congruent to ones identified in vitro (Extended Data Fig. 6b). GSEA of a customized pathway derived from the *Tet2* KO versus WT comparison in *Dnmt3a* KO cells within the resident-like macrophage population, analogous to the BMDM analysis (Fig. 2d), was used to statistically confirm concordance between the two mutant macrophage populations in vivo (Extended Data Fig. 6c). In addition, direct differential gene expression analysis between the mutant genotypes showed that far fewer genes were differentially expressed between *Dnmt3a* KO and *Tet2* KO than between the individual mutants and WT, and that the effect size (fold-change) of the few differentially expressed genes was smaller (Extended Data Fig. 6d).

To validate the expansion of this specialized tissue-resident macrophage population on the level of the surface proteome, we developed a 14-color flow cytometric panel (Extended Data Fig. 7c) and performed flow cytometry on aortic single-cell suspensions at 14 weeks on the diet. This approach confirmed significant expansion of donor-derived TR macrophages in both *Dnmt3a* and *Tet2* mutant myeloid populations (Fig. 4e).

CHIP alters the spatial and proteomic composition of atheromata

The spatial organization of immune cells in tissues is key to their function. To localize the aberrant CHIP-TR macrophage population, we

performed multiplexed ion beam imaging by time of flight (MIBI-TOF) using lanthanide-conjugated antibodies³⁰ on aortic roots after 5 weeks on a western diet, and on aortic arches after 17 weeks on western diet. This high-dimensional imaging technique allowed for simultaneous detection of 28 canonical markers at high resolution (Extended Data Fig. 8a and Supplementary Table 6). A logical 'gating' strategy reminiscent of flow cytometry (Extended Data Fig. 8b) then allowed us to identify the different cell populations that occupy the intima, media, adventitia and cardiac muscle layers with high spatial and phenotypic resolution, and delineate cells of donor or host origin (Fig. 5a and Extended Data Fig. 9b). We identified cells as smooth muscle, endothelium, B cells, T cells, TR macrophages, inflammatory macrophages, lipid-associated macrophages or other myeloid cells. In mice transplanted with 100% *Dnmt3a* or *Tet2* KO bone marrow, we observed an increased density of CD206⁺ resident-like macrophages in the arterial adventitia adjacent to the intimal plaque in both *Dnmt3a* and *Tet2* KO (Fig. 5b and Extended Data Fig. 9a), consistent with the single-cell transcriptomic and flow cytometry data. We additionally validated this finding by classic immunohistochemistry (IHC; Extended Data Fig. 9c). Of note, the presence of both inflammatory and lipid-processing macrophages in the intima (Extended Data Fig. 9b) indicated active myeloid cell infiltration into atheromata, although our ability to unambiguously define inflammatory macrophages was limited because cytokine expression profiles are challenging to capture by MIBI. Of note, we did not detect relevant infiltration of atheromata by CD206⁺ macrophages in the 5-week roots or the 17-week arches, even though scattered CD206⁺ macrophages could be found outside the adventitia and, as expected, there were many in the myocardium³¹. In line with our scRNA-seq and flow cytometry data, MIBI further showed a significant reduction in T cell density in the 5-week roots of mice transplanted with *Dnmt3a* KO marrow (Supplementary Fig. 3).

MIBI further enabled distance analysis between individual cells. Consistent with their unique chemokine signature, TR macrophages lacking *Dnmt3a* or *Tet2* were surrounded by significantly increased numbers of clusters of activated endothelium (defined as CD31⁺CD105⁺ nonhematopoietic cells; Extended Data Fig. 8b) and other myeloid cells (defined as myeloid cells not belonging to the three major macrophage populations; Extended Data Fig. 8b) within the adventitia compared with WT cells (Fig. 5c). This finding agrees with the scRNA-seq cytokine expression profile and supports a functional role for these cells in attracting inflammatory and atherogenic cells to the localized regions of the vascular wall.

Discussion

The present study shows that biallelic loss of *Dnmt3a* in myeloid cells increases atherosclerosis. We went on to identify broad global changes to the myeloid cell transcriptome and atheroma cellular composition on acquisition of mutations in either of the two most commonly mutated genes in CHIP, a recently recognized age-related condition that promotes cardiovascular disease independently of traditional risk factors.

We demonstrated, in the present study of bone marrow chimeric mice, a causal relationship between loss of *Dnmt3a* in myeloid cells and accelerated atherosclerosis, similar to what we reported with *Tet2*. In vitro, we identified a concordant proinflammatory gene expression with deficiency of either gene. These findings fit into the inflammation concept of heart disease³² and suggest a common mechanism by which loss of either epigenetic modifier accelerates atherosclerosis. In addition to important commonalities between loss of *Dnmt3a* and *Tet2*, our analysis also identified some differences. For instance, *Dnmt3a*, but not *Tet2*, KO macrophages showed a significant enrichment of the KEGG pathway 'Osteoclast differentiation', consistent with a recent study showing that *Dnmt3a*-mutated clonal hematopoiesis promotes osteoporosis³³. A small number of pathways were also enriched only in *Tet2* KO macrophages, including the 'Chemokine signaling pathway', reflecting the higher degree of increase in chemokine expression in

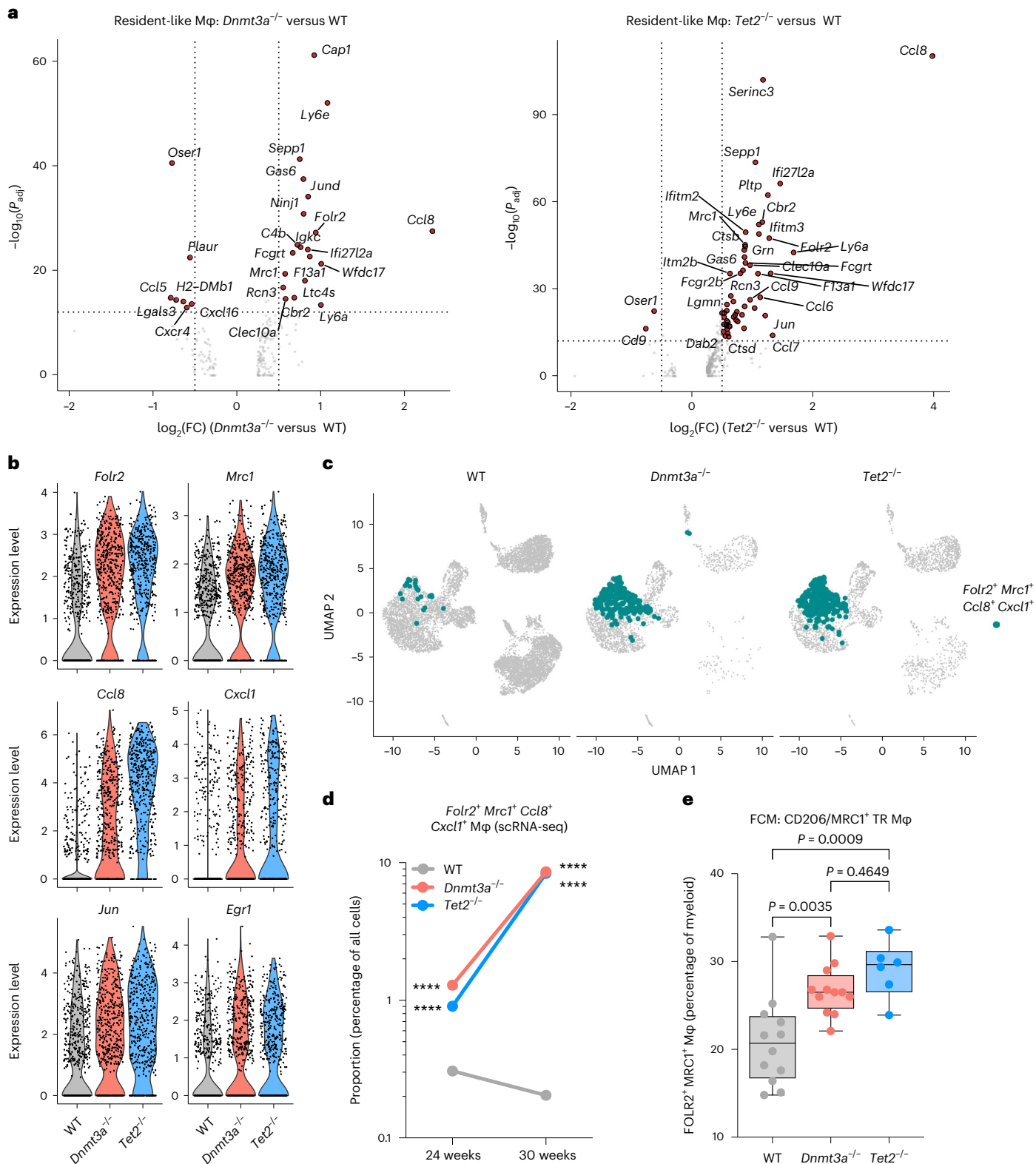


Fig. 4 | *Dnmt3a* and *Tet2* CHIP give rise to a distinct macrophage population that merges a TR phenotype with a chemotactic signature. **a**, Volcano plots depicting differential gene expression analysis in *Dnmt3a*^{-/-} versus WT (left) and *Tet2*^{-/-} versus WT (right) within the resident-like macrophage (Mφ) cluster using the FindMarkers function in Seurat ($\log_2(\text{FC})$ threshold = 0.25) and a negative binomial generalized linear model. Labeled are genes with a $\log_2(\text{FC}) > 0.5$ (vertical lines) and adjusted P value $< 10 \times 10^{-12}$ (horizontal line). **b**, Violin plots contrasting single-cell expression of key individual genes enriched in CHIP across genotypes, within the resident-like Mφ population. **c**, *Folr2*⁺ *Mrc1*⁺ *Ccl8*⁺ *Cxcl1*⁺ (CHIP-TR) macrophages highlighted on a UMAP plot in turquoise (gray dots correspond to all other cells), separated by genotype, after 30 weeks of a high-fat, high-cholesterol diet. **d**, Proportion of CHIP-TR macrophages in the aorta at 24 and 30 weeks by scRNA-seq. A two-sided Fisher's exact test was used with the WT as the control population. **** $P < 0.0001$. **e**, TR Mφs within the myeloid cell population by flow cytometry ($n = 12$ female mice for WT and *Dnmt3a*^{-/-} and $n = 6$ for *Tet2*^{-/-} group). One-way analysis of variance (ANOVA) with Tukey's post-hoc test was used. The box plots show minimum, 25th percentile, median, 75th percentile and maximum.

(CHIP-TR) macrophages highlighted on a UMAP plot in turquoise (gray dots correspond to all other cells), separated by genotype, after 30 weeks of a high-fat, high-cholesterol diet. **d**, Proportion of CHIP-TR macrophages in the aorta at 24 and 30 weeks by scRNA-seq. A two-sided Fisher's exact test was used with the WT as the control population. **** $P < 0.0001$. **e**, TR Mφs within the myeloid cell population by flow cytometry ($n = 12$ female mice for WT and *Dnmt3a*^{-/-} and $n = 6$ for *Tet2*^{-/-} group). One-way analysis of variance (ANOVA) with Tukey's post-hoc test was used. The box plots show minimum, 25th percentile, median, 75th percentile and maximum.

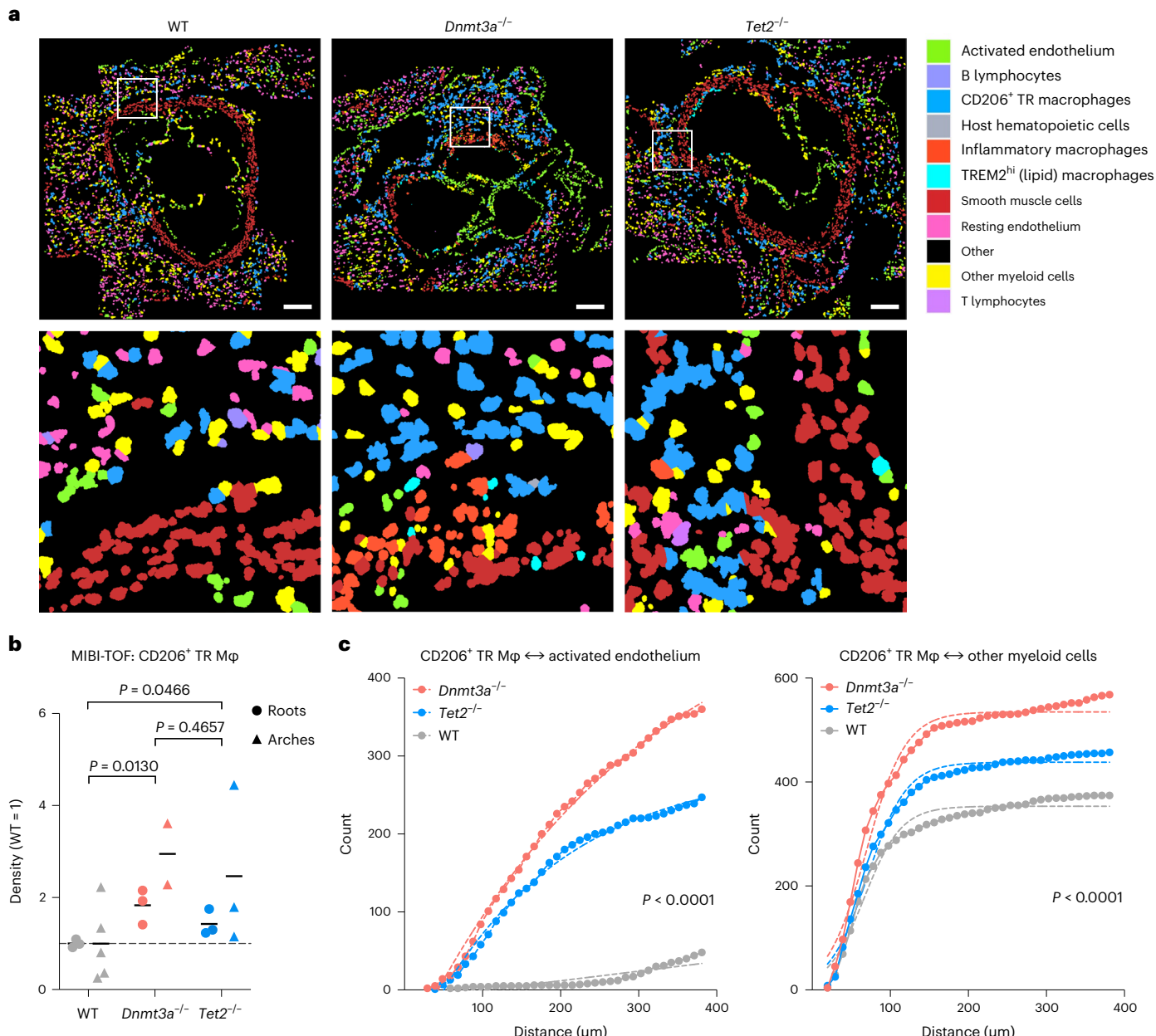


Fig. 5 | Loss of *Dnmt3a* or *Tet2* in hematopoietic cells alters the spatial cellular composition of atheromata. **a**, Cell identity maps of aortic roots in female *Ldlr*^{-/-} mice transplanted with WT, *Dnmt3a*^{-/-} or *Tet2*^{-/-} marrow after 5 weeks on a western diet, generated by MIBI-TOF. Color-coded cell identities obtained by MIBI via the decision tree shown in Extended Data Fig. 8b are overlaid on to the segmentation mask. Scale bars, 200 μm. The white squares indicate areas of the adventitia depicted at high power in the bottom row. **b**, Density of adventitial CD206⁺ TR Mφs in WT, *Dnmt3a*^{-/-} and *Tet2*^{-/-} by MIBI-TOF. Data from $n = 19$ individual animals from 2 cohorts are shown, each cohort normalized to WT: 5-week roots (circles), 17-week

arches (triangles). For quantification strategy, see Extended Data Fig. 9a and Supplementary Fig. 2b. Scatter dot plot is shown with lines at the mean. A two-way ANOVA was used: $P = 0.0439$ for genotype effect, $P = 0.1402$ for sample-type effect. Pairwise comparisons for genotypes were calculated using Tukey's contrasts and univariate P values were reported. **c**, Number of adventitial CD206⁺ TR Mφs with at least three cells of interest (activated endothelium or other myeloid cells) within an expanding distance in 5-week roots. The P values are obtained by an extra-sum-of-squares F test comparing best-fit values obtained by nonlinear regression analysis (dashed lines).

Tet2 versus WT compared with *Dnmt3a* KO versus WT (Extended Data Fig. 4b).

ScRNA-seq revealed the emergence of a distinct macrophage subset in vivo, observed only within *Dnmt3a* or *Tet2* KO populations, providing key insight into the mechanism by which CHIP accelerates atherosclerosis. This macrophage population derives from a blood-borne precursor, yet preferentially occupies the adventitia, a niche typically devoid of monocyte-derived macrophages, indicating that mutant cells may be better at repopulating this niche. Data presented

in the present study indicate that these aberrant macrophages differentially alter their surrounding tissue by secreting potent signaling molecules that activate endothelium and attract other immune cells (CCL2, CCL7, CCL8, CXCL1 and CXCL10). Collectively, these events may lead to larger atherosclerotic plaques that harbor more inflammatory macrophages capable of exacerbating the plaque's growth (Extended Data Fig. 10). In particular, the gene expression signature of this macrophage subpopulation supports strikingly pathogenic qualities: proinflammatory and preferentially infiltrative. Thus, we hypothesize

that selective depletion of the population may reduce accelerated atherogenesis associated with CHIP, although an experimental model depleting these cells is needed to test this hypothesis. Although targeting cells of the innate immune system to achieve atheroprotective effects carries the risk of jeopardizing host defense³⁴, the exclusive expansion of this population in CHIP carriers renders it an attractive target. A recently published subgroup analysis of the phase 3 CANTOS trial revealed that the achieved reduction in recurrent cardiovascular events with anti-IL-1 β therapy³⁵ was largely attributable to patients with CHIP²¹, highlighting the potential of targeting proinflammatory cell populations to positively impact outcomes in these individuals.

Our single-cell sequencing analysis highlighted additional changes, including a marked reduction in the plaque T cell population and a shift in the relative contribution of T cell subsets in mutants, particularly *Dnmt3a*^{-/-}. As the WT T cell population in the same animals is not diminished, we concluded that this effect was cell intrinsic and due to the mutant genotype; the exact underlying mechanisms and phenotypic consequences will require further study.

Mechanistically, despite exerting opposite catalytic functions, loss of *Dnmt3a* or *Tet2* function leads to a myriad of convergent downstream transcriptomic and cellular changes. Conceptually, one possible explanation for this may be that loss of either gene can decrease the level of 5-hydroxymethylcytosine, a cytosine derivative downstream of both *Dnmt3a* and *Tet2* activity that may play a role in regulating transcription³⁶; however, the exact mechanism underlying the convergent transcriptomic changes is currently elusive and will require further subcellular mechanistic studies. Of interest, a recent study showed that both *DNMT3A* and *TET2* function to maintain mitochondrial DNA integrity and restrain the type I interferon response in human monocyte-derived macrophages³⁷.

Notably, *Dnmt3a* accelerates atherosclerosis only when homozygously inactivated in mice. Although this finding stands in apparent contrast to the situation in humans with CHIP, who typically bear only one mutated allele, it is worth noting that the most common *DNMT3A* mutation in position Arg882 exerts a dominant negative effect on the WT allele and this phenomenon may also occur due to other missense variants in the gene^{38–40}. Furthermore, patients with hematological malignancies and CHIP not infrequently carry biallelic loss-of-function mutations in *DNMT3A*^{41,42} and biallelic mutations in *DNMT3A* are the most common co-mutation type in CHIP². In addition, data from large human cohorts suggest milder cardiovascular disease manifestations in individuals with mutations in *DNMT3A* compared with *TET2* (refs. 13,43). Thus, these mouse experiments may not have sufficient sensitivity to detect the effect of heterozygous deficiency in *Dnmt3a* function, in contrast to the phenotype seen with *Tet2* (refs. 13,17).

Another interesting observation in the present study is that plaque size in advanced atherosclerosis is similar between *Dnmt3a* KO and WT, in line with a diminishing effect size over time for *Tet2* KO¹³. This further supports our proposed mechanism: early on in lesional development when recruitment dominates¹⁸, *Dnmt3a* or *Tet2* KO chemokine-enriched, tissue-resident macrophages attract more myeloid cells to the lesions. This leads to larger lesions and their cellular composition is higher in macrophages (Fig. 1). One clinical correlate of this may be the observation that patients with lesions rich in macrophages were more likely to have adverse outcomes⁴⁴. Later in lesional development local proliferation dominates and recruitment becomes less important¹⁸. In advanced lesions, we did not find differences in macrophage cycling across WT, *Dnmt3a* and *Tet2* KO (Extended Data Fig. 5f), consistent with a minimal difference in plaque size at these timepoints between mutant and WT engrafted mice.

Ongoing efforts in our laboratory and by others examining the molecular underpinnings of cardiovascular inflammation associated with CHIP mutations other than those affecting *DNMT3A* and *TET2* have and will continue to add important further information on common and divergent features of inflammation in CHIP⁴⁵. Of particular interest,

a recently published study exploring the mechanism of accelerated atherosclerosis in the context of mutated *Jak2*, known to confer a substantially higher cardiovascular disease risk in humans, described a mechanism distinct from our findings for *Dnmt3a* and *Tet2* (ref. 22).

In conclusion, our data demonstrate concordant phenotypic changes at the transcriptomic, cellular, spatial and organismic level with loss of either *Dnmt3a* or *Tet2*, accelerating the occurrence and progression of atherosclerosis. We further identify a distinct macrophage population specific to the CHIP context with composite properties that position these cells as important contributors to the development of atherosclerotic cardiovascular disease. The application in the present study of single-cell transcriptomics in combination with spatial proteomics provides insight into the mechanisms by which CHIP promotes atherosclerosis. Our findings support the targeting of dysregulated inflammatory pathways as a promising therapeutic strategy to mitigate the deleterious consequences of this widespread, aging-associated condition with unmet medical need.

Methods

Animal husbandry

The Institutional Animal Care and Use Committees of Brigham and Women's Hospital (protocol no. 2017N000060) and the Dana-Farber Cancer Institute (protocol no. 19-008) granted approval for all mouse experiments as described in the present study. All animals used in these experiments were housed with a standard light:dark 12 h:12 h schedule and had free access to food and water. In line with the National Institutes of Health (NIH) Guide Notice NOT-OD-15-102, both male and female mice were used in the present study, as noted above in individual experiments.

Strains used in the present study include the *Dnmt3a*-floxed line B6;129S-Dnmt3atm1.1Jae/J⁴⁶, *Tet2*-floxed line B6;129S-Tet2tm1.1laai/J (Jax, catalog no. 017573)⁸, the hypercholesterolemia-prone *Ldlr* KO line B6;129S7-Ldlrtm1Her/J (Jax, catalog no. 002207) and B6.SJL-Ptprca Pepcb/BoyJ (CD45.1 $^+$). Mice with constitutive expression of Cre recombinase under control of either the *Vav1* promoter (B6.Cg-Tg(*Vav1*-cre) A2Kio/J (Jax, catalog no. 008610)) or the *LysM* promoter (B6.129P2-Lyz2tm1(cre)Ifo/J (Jax, catalog no. 004781)) were crossed with the *Dnmt3a*- or *Tet2*-floxed line to generate animals with *Dnmt3a* or *Tet2* KO specific to the entire hematopoietic or myeloid lineage, respectively. Where appropriate, WT *Vav1*-Cre or *LysM*-Cre animals were used as controls. *Ldlr*^{-/-} mice were crossed with B6.SJL-Ptprca Pepcb/BoyJ (Jax, catalog no. 002014) to generate *Ldlr*^{-/-} mice homozygous for the pan-leukocyte marker CD45.1 (CD45.1 *Ldlr*^{-/-}), which were used as transplant recipients.

Genotyping

All alleles were genotyped by Transnetyx, Inc. In-house verification of genotyping was performed by PCR analysis of peripheral blood DNA after harvest. *Tet2* PCR used a three-primer reaction with an annealing temperature of 61 °C for 30 cycles. The PCR primers are TAGAGG GAGGGGGCATAGT (LOXP3R), AAGAATTGCTACAGGCCTGC (Flox F) and TTCTTAGCCCTTGCTGAGC (Flox R). This assay distinguishes the WT allele (248 bp), the floxed allele (480 bp) and the excised allele (580 bp). *Dnmt3a* PCR used a three-primer reaction and a touchdown PCR protocol: starting with 68 °C annealing temperature, decreasing by 1 °C per cycle for 10 cycles, then continuing with 58 °C annealing for 24 more cycles. The PCR primers are GATTGCTACAGGTGAGTGGCATG (D3a1Lox6), GGTCTTCAGGTTATTCCGGTG (D3a1Lox5) and GGAGGT TACCCCGAGTAACG (D3aCommon2). This assay distinguishes the WT allele (220 bp), the floxed allele (330 bp) and the excised allele (420 bp).

Bone marrow transplantation

Recipient *Ldlr* KO CD45.1 $^+$ mice were lethally irradiated with two doses of γ -irradiation (475 cGy) separated by 4 h. Donor CD45.2 $^+$ bone marrow

was obtained from *Dnmt3a*^{+/+}, *Dnmt3a* flox/flox, *Tet2*^{+/+} or *Tet2* flox/flox littermates and (competitor) CD45.1⁺ bone marrow was obtained from WT CD45.1⁺ mice. Post-irradiation, recipients were transplanted with 2×10^6 whole bone marrow cells in suspension via retro-orbital injection. After transplantation, recipient mice were provided with sterilized cages, food and water for a period of 4 weeks. Water was supplemented with antibiotic (trimethoprim–sulfamethoxazole) for the first 3 weeks after transplantation.

Modeling hypercholesterolemia

At 4 weeks post-transplantation, mice were started on a high-fat, high-cholesterol diet (Harlan-Teklad, catalog no. TD.96121; 21% milkfat, 1.25% cholesterol diet). This hypercholesterolemia-promoting regimen was continued for the specified durations, as noted above.

Analysis of peripheral blood

Blood was collected from mice via the retro-orbital sinus into EDTA collection tubes at the timepoints specified above. This EDTA-anticoagulated whole blood was run on an Advia 2120 hematology system to obtain a complete blood count. Chimerism for CD45 isoforms and cellular subpopulations were identified by flow cytometry on a FACS-CANTO II (Becton Dickinson) using FITC-conjugated anti-CD45.1 (clone A20, BD Biosciences), allophycocyanin (APC)-conjugated anti-CD45.2 (clone 104, BioLegend), Pacific Blue-conjugated anti-CD11b (clone M1/70, Invitrogen), phycoerythrin (PE)-conjugated anti-CD3 (clone 17A2, BD Biosciences), PE-Cy7-conjugated anti-CD19 (clone 1D3, BD Biosciences), PerCP-eFluor 710-conjugated anti-Ly-6G (clone 1A8, Invitrogen) and APC-Cy7-conjugated anti-CD115 (clone AFS98, BioLegend). For characterization of lipids or proteins, immediately before euthanization, peripheral blood samples from overnight-fasted mice were obtained by terminal bleeding via the retro-orbital sinus. Serum was isolated from EDTA-free blood and frozen at -80°C . Lipid measurements were performed by Charles River Laboratories.

Quantification of atherosclerosis and histological analysis of organs

Serial cryostat sections of aortic root ($6\text{ }\mu\text{m}$) were cut from optimal cutting temperature-embedded, unfixed hearts at the level of the aortic valves and stored at -80°C until use. For quantification of lesion size, aortic root sections were stained with Oil Red O (ORO; Sigma-Aldrich, catalog no. O0625), a lipophilic red dye, to assess plaque accumulation. Sections were counterstained with Gill's hematoxylin solution (Sigma-Aldrich) and mounted using water-soluble mounting medium (glycerol–gelatin, Sigma-Aldrich). Images of the roots were acquired using a Nikon Eclipse E400 microscope. Quantification of aortic root lesion area was performed using ImageJ (<http://rsb.info.nih.gov/ij/index.html>) on five or six adjacent, ORO-stained cryostat sections. The individual performing this analysis was blinded to the genotype of the samples. The total lesion area on each slide was then averaged to obtain a mean lesion area per mouse. IHC was performed using purified rat anti-mouse CD68 antibody (clone FA-11, BioLegend) or a CD206/MRC1 rabbit monoclonal antibody. Staining with appropriate biotinylated secondary antibodies (Vector) was followed by incubation with streptavidin–horseradish peroxidase (Dako or Vector). Stains were developed using 3-amino-9-ethylcarbazole (Abcam) or 3,3'-diaminobenzidine (DAB; Vector) followed by a hematoxylin-based nuclear counterstain. Images were acquired using a Revolve Fluorescence Microscope (Echo Labs). The CD68⁺ area was manually quantified using FIJI/ImageJ2 (v.2.3.0/1.53t) and expressed as a percentage of the total lesion area. For CD206, we first performed color segmentation in FIJI to isolate the DAB-positive areas along a section of the vascular wall, avoiding any areas of myocardium. We then calculated the integrated DAB density. The obtained value was normalized to the (arc) length of the analyzed section. Connective tissue was visualized using Masson's Trichrome staining protocol, images were acquired using a Revolve Fluorescence

Microscope (Echo Labs), and the collagen cap area was manually quantified using FIJI/ImageJ and expressed as a percentage of the total lesion area. Statistical comparisons between groups was performed using Welch's *t*-test, with a pre-specified significance threshold of $P < 0.05$.

Flow cytometric analysis of atherosclerotic plaques

Aortae were perfused with 20 ml of cold phosphate-buffered saline (PBS), followed by careful dissection from the surrounding tissues. Aortic tissue (from the sinotubular junction to the bifurcation) was cut into small pieces and subjected to enzymatic digestion with 450 U ml^{-1} of collagenase I, 125 U ml^{-1} of collagenase XI, 60 U ml^{-1} of DNase I and 60 U ml^{-1} of hyaluronidase (Sigma-Aldrich) for 1 h at 37°C while shaking. The resulting cell suspension was passed through a 70- μm filter, followed by staining with multi-color panels using combinations of the following monoclonal antibodies: Brilliant Violet 510-conjugated anti-CD11b (clone M1/70, BioLegend), Brilliant Violet 605-conjugated anti-F4/80 (clone BM8, BioLegend), Brilliant Violet 650-conjugated anti-CD45.2 (clone 104, BioLegend), Brilliant Violet 711-conjugated anti-Ly6G (clone 1A8, BD Biosciences), Brilliant Violet 786-conjugated anti-CD16/32 (clone 93, BD Biosciences), Alexa Fluor-488-conjugated, anti-Lyve1 (clone ALY7, eBioscience), PE-conjugated anti-Ly6C (clone HK1.4, eBioscience), PerCP-Cy5.5-conjugated anti-CD3 (clone 17A2, BioLegend), APC-conjugated anti-CD206 (clone C068C2, BD Biosciences), PE-conjugated anti-FOLR2 (clone 10/FR2, BioLegend), Alexa Fluor-700-conjugated anti-CD19 (clone 6D5, BioLegend) and APC-Cy7-conjugated anti-CD11c (clone N418, BioLegend). Data acquisition was performed on a BD LSR Fortessa flow cytometer and analysis was carried out using FlowJo v.10.8.2.

Generation of BMDMs

Whole bone marrow was isolated from the long bones, hips and vertebrae of 10- to 14-week-old mice by crushing and sequential passage through 70- μm and 40- μm cell strainers (Corning, catalog nos. 352350 and 352340). Red cell lysis with $1\times$ PharmLyse (BD Biosciences, catalog no. 555899) was performed and bone marrow was cultured by creating a single-cell suspension of whole bone marrow in Iscove's modification of Dulbecco's modified Eagle's medium (IMDM) (Corning, catalog no. 10016CV) supplemented with 10% fetal bovine serum (FBS) (Omega Scientific, catalog no. FB-11), 10 ng ml^{-1} of recombinant mouse macrophage-colony-stimulating factor (M-CSF; Miltenyi Biotec, catalog no. 130-101-706) and 1% penicillin–streptomycin–glutamine (PSG) (Gibco, catalog no. 10378-016) in a 30-ml total volume. After 3 d, each dish was supplemented with 15 ml of the above medium and macrophages were harvested on day 6 with a cell lifter.

Stimulation of BMDMs

BMDMs were grown as described above and harvested on day 6 of culture and re-plated into 48-well plates (750,000 cells per well) in IMDM with 10% FBS, 1% PSG and 10 ng ml^{-1} of M-CSF. After 24 h, the medium was replaced with medium containing LDL or vehicle as described below.

Human LDL (Ifa Aeser, catalog no. BT-903) was resuspended to a final concentration of 200 mg dl^{-1} , along with 10% FBS, 1% PSG and 10 ng ml^{-1} of recombinant mouse M-CSF into $1\times$ IMDM from powdered stock (Life Technologies, catalog no. 12200036). For vehicle-treated samples, LDL was replaced with 0.05 M Tris-HCl buffer, with 0.15 M NaCl and 0.3 mM EDTA, pH 7.4 in the above mixture.

Intracellular flow cytometry

BMDMs were grown in six-well plates (2×10^6 cells per well) as described above, and the medium was changed on days 3 and 6. For intracellular flow cytometry, lipopolysaccharide stimulation was followed by treatment with the Golgi body inhibitor Brefeldin A, followed by fixation and permeabilization using a paraformaldehyde–saponin-based Fixation/Permeabilization kit (BD Biosciences). The cells were then stained for

pro-IL-1 β using a PE-Cy7 or PE-conjugated monoclonal antibody (clone NJTEN3, Life Technologies). We validated this antibody clone for this specific application using an appropriate isotype control (clone eBGRG1).

ELISA

ELISA for chemokines/cytokines was performed on BMDM supernatants after 24 h of LDL stimulation using commercially available kits, according to the manufacturer's instructions: mouse CXCL1 (Abcam, catalog no. ab100717), mouse CXCL2 (Abcam, catalog no. ab204517), mouse CXCL3 (Abcam, catalog no. ab206310) and mouse IL-6 (R&D Systems, catalog no. M6000B).

RNA-seq

BMDMs were treated with LDL or vehicle as described above and harvested after 24 h using TRIzol reagent (Invitrogen, catalog no. 15596026). RNA was purified using RNeasy Mini columns (QIAGEN, catalog no. 74104) followed by DNase treatment (TURBO DNA-free Kit, Life Technologies, catalog no. AM1907). Ribo-Zero Kit (Illumina, catalog no. MRZH116) was used to eliminate ribosomal RNA. Library preparation using a poly(A) selection, multiplexing and sequencing on two HiSeq2500 lanes was done by Genewiz. A total of 34 BMDM samples derived from mice of four genotypes (*Dnmt3a*^{-/-}, *Jak2*^{WT}, *Tet2*^{-/-} and WT) subjected to two conditions (LDL treated and untreated) were analyzed for the present study. The sample set contained *Tet2*^{-/-} samples that were harvested at a different time along with their respective matched WT controls and also used for a previous publication¹³, identified by the suffix 'batch 1' in Gene Expression Omnibus, accession no. [GSE237599](https://www.ncbi.nlm.nih.gov/geo/query/acc.cgi?acc=GSE237599). This set was used for the comparative analyses in Fig. 2a and Extended Data Figs. 3a,b and 4b, whereas the concordance analyses in Fig. 2c,d used *Tet2*^{-/-} samples generated for the present study. Reads were mapped to the *Mus musculus* mm10 reference genome with the CLC Genomics Server program v.9.0.1. Normalized read counts were obtained from the resulting BAM files using the BioLite (<https://bioconductor.org/biocLite.R>) package in R. Differential gene expression was analyzed using the DESeq2 (<https://bioconductor.org/packages/release/bioc/html/DESeq2.html>) package in R considering the effect of LDL treatment and genotype as separate variables in a linear model (design = ~ genotype + treatment). Genes were assigned P values based on being differentially expressed owing to genotype, and separate P values were obtained for differential expression based on treatment. Genes with $P < 0.05$ were considered significant in each respective analysis. GSEA was performed using the Broad GSEA pipeline and the R packages clusterProfiler, Enrichr and fgsea^{47–49}.

FACS for scRNA-seq

Aortic single-cell suspensions were generated as described above, followed by staining with CD45.1-FITC (clone A20, BioLegend) and CD45.2-APC (clone 104, BioLegend). Viable, single aortic leukocytes were sorted with a 100- μ m nozzle using a BD FACS Aria (BD Biosciences) into 1× PBS with 0.4% bovine serum albumin. Post-sort analysis indicated a purity of consistently >99%.

Droplet-based scRNA-seq

Sorted aortic leukocyte suspensions were loaded on the chromium single-cell controller (10 \times Genomics) to generate a single-cell and gel bead emulsion (GEM). An input of 7,000 cells was added to each channel of a chip with a recovery rate of 3,500 cells on average. ScRNA-seq libraries were prepared using the Single Cell 3' Solution v.2 Reagent Kit, following the manufacturer's protocol and as described previously⁵⁰. Libraries were sequenced on an Illumina NextSeq 500.

Computational analysis of scRNA-seq data

The BCL files were demultiplexed using 8-bp 10 \times sample indexes and 'cellranger mkfastq' to generate paired-end FASTQ. We ran 'cellranger count' to align the reads to the mouse UCSC mm10 reference genome

using STAR aligner, as well as perform filtering, barcode counting and unique molecular identifier counting. The alignment results were used to quantify the expression level of mouse genes and generation of gene–barcode matrix. Each sample's cellranger matrix was then loaded in a SeuratObject 4.1.0 using Seurat 4.1.1 (<https://github.com/satijalab/seurat>). The R code used for further analysis is available on GitHub and summarized below.

QC and filtering parameters. Low-quality cells, doublets and potential dead cells were removed according to the percentage of mitochondrial genes and number of genes expressed in each cell (nFeature_RNA > 200 & nFeature_RNA < 4400 & percent.mt < 15). Filtering parameters were based on visualized QC metrics using the percent.mt/nCount_RNA and nFeature_RNA/nCount_RNA plots.

Normalization, variable feature selection, scaling and linear dimensionality reduction. Samples were then normalized using a global-scaling normalization method called LogNormalize. Using the FindVariableFeatures function, the top 2,000 most highly variable genes were identified and used for downstream analysis to highlight biological signal. Cell-cycle scores were assigned using Seurat's CellCycleScoring function. Linear transformation scaling was performed to prepare the data for dimensional reduction techniques. Cell-cycle scores were regressed out during data scaling, followed by principal component analysis.

Integration and clustering. The different objects were then integrated using Harmony (<https://github.com/immunogenomics/harmony>). Based on the ElbowPlot, we selected eight significant dimensions to cluster the cells. Dimensionality reduction via Unifold Manifold Approximation and Projection (UMAP) embedding was performed on the integrated dataset, followed by the FindNeighbors and FindClusters functions.

Doublet detection. Doublet detection and removal was performed on the 30-week dataset using doubletFinder_v3 (<https://github.com/chris-mcginnis-ucsf/DoubletFinder>).

Downstream analysis and data visualization. Identities of the cell clusters were determined using canonical cell-type markers. For identification of cluster signature genes, we used the FindAllMarkers function in the Seurat package with Wilcoxon's rank-sum test, testing genes that were detected in at least 25% of cells in either of the two groups with at least a 0.25 difference (log-scale) between the two groups, and at least three cells expressing the feature in at least one of the two groups. Differential gene expression within the resident-like macrophage cluster was calculated using the FindMarkers function, with a negative binomial generalized linear model. We tested genes that were detected in at least 10% of cells in WT or mutant populations, with at least a 0.25 difference (log-scale) between the two groups of cells and at least three cells expressing the feature in at least one of the two groups. The difference between the proportion of cell types across different samples was calculated by a proportion test using the Single Cell Proportion Test R package (<https://github.com/rpolicastro/scProportionTest>).

Analysis of the 24-week dataset. For the 24-week dataset, an analogous analysis was performed with three modifications: (1) filtering parameters were nFeature_RNA > 300 & nFeature_RNA < 4500 & percent.mt < 15, again based on visualizing QC metrics; (2) we used sctransform-based normalization; and (3) we selected 11 dimensions to cluster the cells, again based on the ElbowPlot.

Multiplexed ion beam imaging time of flight

Antibody preparation. Antibodies were conjugated to isotopic metal reporters as described previously³⁰. The following conjugation antibodies were diluted in Candor PBS Antibody Stabilization solution

(Candor Bioscience). Antibodies were either stored at 4 °C or lyophilized in 100 mM D-(+)-trehalose dehydrate (Sigma-Aldrich) with ultrapure distilled H₂O for storage at -20 °C. Before staining, lyophilized antibodies were reconstituted in a buffer of Tris (Thermo Fisher Scientific), sodium azide (Sigma-Aldrich), ultrapure water (Thermo Fisher Scientific) and antibody stabilizer (Candor Bioscience) to a concentration of 0.05 mg ml⁻¹. Information on the antibodies, metal reporters and staining concentrations is located in Supplementary Table 6.

Tissue staining. Mouse aortic roots were embedded directly into optimal cutting temperature and fresh frozen. They were then sectioned (6-μm section thickness) from tissue blocks on to gold- and tantalum-sputtered microscope slides. After sectioning, slides were immediately placed in a 10% formalin bath for 10 min. Then, slides were washed 3× for 5 min in 1× PBS IHC Washer Buffer with Tween-20 (Cell Marque) and 0.1% (w:v) bovine serum albumin (Thermo Fisher Scientific). Tissues were then blocked for 1 h at room temperature with 1× tris-buffered saline IHC Wash Buffer with Tween-20 and 3% (v:v) normal donkey serum (Sigma-Aldrich), 0.1% (v:v) cold fish skin gelatin (Sigma-Aldrich), 0.1% (v:v) Triton X-100 and 0.05% (v:v) sodium azide. The first antibody cocktail was prepared in 1× tris-buffered saline IHC Wash Buffer with Tween-20 with 3% (v:v) normal donkey serum and filtered through a 0.1-μm centrifugal filter (Millipore) before incubation with tissue overnight at 4 °C in a humidity chamber. Afterwards, the overnight incubation slides were washed twice for 5 min in wash buffer. The second-day antibody cocktail was prepared as described and incubated with the tissues for 1 h at 4 °C in a humidity chamber. After staining, slides were washed twice for 5 min in wash buffer and fixed in a solution of 2% glutaraldehyde (Electron Microscopy Sciences) solution in low-barium PBS for 5 min. Slides were washed in PBS (1×), 0.1 M Tris at pH 8.5 (3×) and ddH₂O (2×) and then dehydrated by washing in 70% ethanol (1×), 80% ethanol (1×), 95% ethanol (2×) and 100% ethanol (2×). Slides were dried under vacuum before imaging.

MIBI-TOF imaging. Imaging was performed using a MIBI-TOF instrument with a Hyperion ion source. Xe⁺ primary ions were used to sequentially sputter pixels for a given field of view. The following imaging parameters were used:

- Pulse setting: medium;
- Field size: 400 μm² at 1,024 × 1,024 pixels²;
- Dwell time: 0.5 ms;
- Median gun current on tissue: 4.11 nA of Xe⁺.

Low-level image processing. MIBI images were processed as previously described³⁰. In brief, multiplexed image sets were extracted, slide background subtracted, denoised and aggregate filtered. All parameters for these steps can be found in Supplementary Table 6.

Cell density analysis. Cell density quantification, expressed as percentage of area, was performed on cell identity maps (5-week roots) or single-channel images (17-week arches) using color segmentation in FIJI/ImageJ2 (v.2.3.0/1.53t), as delineated in Extended Data Fig. 9a and Supplementary Fig. 2b.

Single-cell segmentation. Nuclear segmentation and localization was performed using DeepCell on aggregate filtered images (<https://deepcell.org>).

Reporting summary

Further information on research design is available in the Nature Portfolio Reporting Summary linked to this article.

Data availability

The data supporting the findings of the present study are available within the paper and Supplementary information and Source data

files. All sequencing data from the present study have been deposited in the National Center for Biotechnology Information Gene Expression Omnibus, accession nos. [GSE225773](https://doi.org/10.3391/GEO225773) for scRNA-seq and [GSE237599](https://doi.org/10.3391/GEO237599) for bulk RNA-seq. The UCSC mm10 reference genome was used for alignment of sequencing data. Multiplexed imaging data has been deposited in Mendeley (<https://data.mendeley.com/datasets/dgyrt473vs/1>).

Code availability

R code used to analyze scRNA-seq data has been deposited in GitHub (<https://github.com/jkgopa/DNMT3A-single-cell>).

References

1. Jaiswal, S. & Ebert, B. L. Clonal hematopoiesis in human aging and disease. *Science* **366**, eaan4673 (2019).
2. Jaiswal, S. et al. Age-related clonal hematopoiesis associated with adverse outcomes. *N. Engl. J. Med.* **371**, 2488–2498 (2014).
3. Nowbar, A. N., Gitto, M., Howard, J. P., Francis, D. P. & Al-Lamee, R. Mortality from ischemic heart disease. *Circ. Cardiovasc. Qual. Outcomes* **12**, e005375 (2019).
4. Smith, Z. D. & Meissner, A. DNA methylation: roles in mammalian development. *Nat. Rev. Genet.* **14**, 204–220 (2013).
5. Bowman, R. L., Busque, L. & Levine, R. L. Clonal hematopoiesis and evolution to hematopoietic malignancies. *Cell Stem Cell* **22**, 157–170 (2018).
6. Ito, S. et al. Role of Tet proteins in 5mC to 5hmC conversion, ES-cell self-renewal and inner cell mass specification. *Nature* **466**, 1129–1133 (2010).
7. Ito, S. et al. Tet proteins can convert 5-methylcytosine to 5-formylcytosine and 5-carboxylcytosine. *Science* **333**, 1300–1303 (2011).
8. Moran-Crusio, K. et al. Tet2 loss leads to increased hematopoietic stem cell self-renewal and myeloid transformation. *Cancer Cell* **20**, 11–24 (2011).
9. Challen, G. A. et al. Dnmt3a and Dnmt3b have overlapping and distinct functions in hematopoietic stem cells. *Cell Stem Cell* **15**, 350–364 (2014).
10. Cimmino, L. et al. Restoration of TET2 function blocks aberrant self-renewal and leukemia progression. *Cell* **170**, 1079–1095.e20 (2017).
11. Pan, W. et al. The DNA methylcytosine dioxygenase Tet2 sustains immunosuppressive function of tumor-infiltrating myeloid cells to promote melanoma progression. *Immunity* **47**, 284–297.e5 (2017).
12. Li, Z. et al. Deletion of Tet2 in mice leads to dysregulated hematopoietic stem cells and subsequent development of myeloid malignancies. *Blood* **118**, 4509–4518 (2011).
13. Jaiswal, S. et al. Clonal hematopoiesis and risk of atherosclerotic cardiovascular disease. *N. Engl. J. Med.* **377**, 111–121 (2017).
14. Bick, A. G. et al. Genetic interleukin 6 signaling deficiency attenuates cardiovascular risk in clonal hematopoiesis. *Circulation* **141**, 124–131 (2020).
15. Sano, S. et al. CRISPR-mediated gene editing to assess the roles of Tet2 and Dnmt3a in clonal hematopoiesis and cardiovascular disease. *Circ. Res.* **123**, 335–341 (2018).
16. Dorsheimer, L. et al. Association of mutations contributing to clonal hematopoiesis with prognosis in chronic ischemic heart failure. *JAMA Cardiol.* **4**, 25–33 (2019).
17. Fuster, J. J. et al. Clonal hematopoiesis associated with TET2 deficiency accelerates atherosclerosis development in mice. *Science* **355**, 842–847 (2017).
18. Robbins, C. S. et al. Local proliferation dominates lesional macrophage accumulation in atherosclerosis. *Nat. Med.* **19**, 1166–1172 (2013).
19. Williams, J. W. et al. Limited proliferation capacity of aortic intima resident macrophages requires monocyte recruitment for atherosclerotic plaque progression. *Nat. Immunol.* **21**, 1194–1204 (2020).

20. Swirski, F. K. et al. Ly-6Chi monocytes dominate hypercholesterolemia-associated monocytosis and give rise to macrophages in atheromata. *J. Clin. Invest.* **117**, 195–205 (2007).
21. Svensson, E. C. et al. TET2-driven clonal hematopoiesis and response to canakinumab: an exploratory analysis of the CANTOS randomized clinical trial. *JAMA Cardiol.* **7**, 521–528 (2022).
22. Fidler, T. P. et al. The AIM2 inflammasome exacerbates atherosclerosis in clonal haematopoiesis. *Nature* **592**, 296–301 (2021).
23. Libby, P., Lichtman, A. H. & Hansson, G. K. Immune effector mechanisms implicated in atherosclerosis: from mice to humans. *Immunity* **38**, 1092–1104 (2013).
24. Butler, A., Hoffman, P., Smibert, P., Papalexi, E. & Satija, R. Integrating single-cell transcriptomic data across different conditions, technologies, and species. *Nat. Biotechnol.* **36**, 411–420 (2018).
25. Stuart, T. et al. Comprehensive integration of single-cell data. *Cell* **177**, 1888–1902.e21 (2019).
26. Zernecke, A. et al. Meta-analysis of leukocyte diversity in atherosclerotic mouse aortas. *Circ. Res.* **127**, 402–426 (2020).
27. Cochaine, C. et al. Single-cell RNA-seq reveals the transcriptional landscape and heterogeneity of aortic macrophages in murine atherosclerosis. *Circ. Res.* **122**, 1661–1674 (2018).
28. Winkels, H. et al. Atlas of the immune cell repertoire in mouse atherosclerosis defined by single-cell RNA-sequencing and mass cytometry. *Circ. Res.* **122**, 1675–1688 (2018).
29. Tacke, F. et al. Monocyte subsets differentially employ CCR2, CCR5, and CX3CR1 to accumulate within atherosclerotic plaques. *J. Clin. Invest.* **117**, 185–194 (2007).
30. Keren, L. et al. A structured tumor-immune microenvironment in triple negative breast cancer revealed by multiplexed ion beam imaging. *Cell* **174**, 1373–1387.e19 (2018).
31. Epelman, S. et al. Embryonic and adult-derived resident cardiac macrophages are maintained through distinct mechanisms at steady state and during inflammation. *Immunity* **40**, 91–104 (2014).
32. Libby, P. The changing landscape of atherosclerosis. *Nature* **592**, 524–533 (2021).
33. Kim, P. G. et al. Dnmt3a-mutated clonal hematopoiesis promotes osteoporosis. *J. Exp. Med.* **218**, e20211872 (2021).
34. Nahrendorf, M. Myeloid cell contributions to cardiovascular health and disease. *Nat. Med.* **24**, 711–720 (2018).
35. Ridker, P. M. et al. Antiinflammatory therapy with canakinumab for atherosclerotic disease. *N. Engl. J. Med.* **377**, 1119–1131 (2017).
36. Wu, H. et al. Genome-wide analysis of 5-hydroxymethylcytosine distribution reveals its dual function in transcriptional regulation in mouse embryonic stem cells. *Genes Dev.* **25**, 679–684 (2011).
37. Cobo, I. et al. DNA methyltransferase 3 alpha and TET methylcytosine dioxygenase 2 restrain mitochondrial DNA-mediated interferon signaling in macrophages. *Immunity* **55**, 1386–1401.e10 (2022).
38. Russler-Germain, D. A. et al. The R882H DNMT3A mutation associated with AML dominantly inhibits wild-type DNMT3A by blocking its ability to form active tetramers. *Cancer Cell* **25**, 442–454 (2014).
39. Kim, S. J. et al. A DNMT3A mutation common in AML exhibits dominant-negative effects in murine ES cells. *Blood* **122**, 4086–4089 (2013).
40. Huang, Y. H. et al. Systematic profiling of DNMT3A variants reveals protein instability mediated by the DCAF8 E3 ubiquitin ligase adaptor. *Cancer Discov.* **12**, 220–235 (2022).
41. Yang, L., Rau, R. & Goodell, M. A. DNMT3A in haematological malignancies. *Nat. Rev. Cancer* **15**, 152–165 (2015).
42. Saiki, R. et al. Combined landscape of single-nucleotide variants and copy number alterations in clonal hematopoiesis. *Nat. Med.* **27**, 1239–1249 (2021).
43. Nachun, D. et al. Clonal hematopoiesis associated with epigenetic aging and clinical outcomes. *Aging Cell* **20**, e13366 (2021).
44. Mokry, M. et al. Transcriptomic-based clustering of human atherosclerotic plaques identifies subgroups with different underlying biology and clinical presentation. *Nat. Cardiovasc. Res.* **1**, 1140–1155 (2022).
45. Andrysk, Z., Sullivan, K. D., Kieft, J. S. & Espinosa, J. M. PPM1D suppresses p53-dependent transactivation and cell death by inhibiting the integrated stress response. *Nat. Commun.* **13**, 7400 (2022).
46. Nguyen, S., Meletis, K., Fu, D., Jhaveri, S. & Jaenisch, R. Ablation of de novo DNA methyltransferase Dnmt3a in the nervous system leads to neuromuscular defects and shortened lifespan. *Dev. Dyn.* **236**, 1663–1676 (2007).
47. Kuleshov, M. V. et al. Enrichr: a comprehensive gene set enrichment analysis web server 2016 update. *Nucleic Acids Res.* **44**, W90–W97 (2016).
48. Yu, G., Wang, L. G., Han, Y. & He, Q. Y. clusterProfiler: an R package for comparing biological themes among gene clusters. *OMICS* **16**, 284–287 (2012).
49. Korotkevich, G. et al. Fast gene set enrichment analysis. Preprint at bioRxiv <https://doi.org/10.1101/060012> (2021).
50. Haber, A. L. et al. A single-cell survey of the small intestinal epithelium. *Nature* **551**, 333–339 (2017).

Acknowledgements

We thank O. Rozenblatt-Rosen (of Genentech, previously Broad Institute) and A. Rotem (of AstraZeneca, previously the Dana-Farber Cancer Institute) for expert advice regarding scRNA-seq and A. Sperling and M. Slabicki (both of the Dana-Farber Cancer Institute) for helpful discussions. We further thank the staff at the Klarman Cell Observatory of the Broad Institute, the Rodent Histopathology Core at Harvard Medical School, the Stanford Research Computing Center and M. Leventhal for technical assistance. Illustrations were created with BioRender. P.J.R. acknowledges funding support from the EvansMDS Foundation and the John R. Svenson Endowed Fellowship. T.N. is supported by the Japan Society for the Promotion of Science Overseas Fellowship. A.E.L. reports funding from the John S. LaDue Memorial Fellowship in Cardiology, the American Society of Hematology Research Training Grant for Fellows and the American College of Cardiology Merck Fellowship in Cardiovascular Disease and the Metabolic Syndrome. M.A. is supported by funding from the NIH (grant nos. 5U54CA20997105, 5DP5OD01982205, 1R01CA24063801A1, 5R01AG06827902, 5UH3CA24663303, 5R01CA22952904, 1U24CA22430901, 5R01AG05791504 and 5R01AG05628705), the Department of Defense (grant no. W81XWH2110143) and other funding from the Bill and Melinda Gates Foundation, the Cancer Research Institute, the Parker Center for Cancer Immunotherapy and the Breast Cancer Research Foundation. P.L. receives funding support from the National Heart, Lung, and Blood Institute (grant nos. 1R01HL134892 and 1R01HL163099-01), the RRM Charitable Fund and the Simard Fund. B.L.E. is an investigator of the Howard Hughes Medical Institute and received funding from the NIH (grant nos. P01CA066996, P50CA206963 and R01HL082945). S.J. is supported by the Burroughs Wellcome Fund, EvansMDS Foundation, Ludwig Center for Cancer Stem Cell Research, Leukemia and Lymphoma Society, Knight Initiative for Brain Resilience, the NIH (grant no. DP2-HL157540) and the Leducq Foundation.

Author contributions

P.J.R., P.L., B.L.E. and S.J. designed the study. P.J.R., J.G., A.J.S., H.A., M.M., T.N., T.R., A.E.L., M.F., D.N.C., A.V., E.S., G.S. and S.J. performed and/or analyzed *in vivo* experiments on atherosclerotic mice, aortic root imaging and flow cytometry. P.J.R., J.G., A.J.S. and S.J. performed and/or analyzed bulk RNA-seq experiments from BMDMs. P.J.R.,

J.G., D.N., K.B.R., E.S. and S.J. performed and/or analyzed scRNA-seq experiments. P.J.R., J.G., M.B., N.V.G., N.F.G., E.F.M., Z.K. and M.G. performed and/or analyzed MIBI-TOF experiments. A.J.S. and S.J. performed and/or analyzed ELISA experiments. S.B. and M.A. supervised MIBI-TOF experiments. P.L., B.L.E. and S.J. supervised the study. P.J.R. wrote the paper with contributions from all authors. S.J. revised the paper.

Competing interests

M.B. is presently a consultant for the company IonPath Inc., which manufactured the MIBI-TOF instrument used in this paper. A.E.L. is a member of TenSixteen Bio, outside of the submitted work. E.M. previously consulted for IonPath Inc. M.A. is a board member and shareholder in IonPath, which develops and manufactures the commercial MIBI-TOF platform. P.L. is an unpaid consultant to, or involved in, clinical trials for Amgen, AstraZeneca, Baim Institute, Beren Therapeutics, Esperion Therapeutics, Genentech, Kancera, Kowa Pharmaceuticals, Medimmune, Merck, Moderna, Novo Nordisk, Novartis, Pfizer and Sanofi-Regeneron. P.L. is a member of the scientific advisory board for Amgen, Caristo Diagnostics, Cartesian Therapeutics, CSL Behring, DalCor Pharmaceuticals, Dewpoint Therapeutics, Eulicid Bioimaging, Kancera, Kowa Pharmaceuticals, Olatec Therapeutics, Medimmune, Novartis, PlaqueTec, TenSixteen Bio, Soley Therapeutics and XBiotech, Inc. P.L.'s laboratory has received research funding in the last 2 years from Novartis, Novo Nordisk and Genentech. P.L. is on the Board of Directors of XBiotech, Inc. and has a financial interest in XBiotech, a company developing therapeutic human antibodies; in TenSixteen Bio, a company targeting somatic mosaicism and CHIP to discover and develop new therapeutics to treat age-related diseases; and in Soley Therapeutics, a biotechnology company that is combining artificial intelligence with molecular and cellular response detection for discovering and developing new drugs, currently focusing on cancer therapeutics. P.L.'s interests were reviewed and are managed by Brigham and Women's Hospital and Mass General Brigham in accordance with their conflict-of-interest policies. B.L.E. has received consulting fees from GRAIL. He is a member of the scientific advisory board and shareholder for Neomorph

Therapeutics, Skyhawk Therapeutics and Exo Therapeutics. B.L.E.'s laboratory has received research funding in the last 2 years from Novartis and Calico. S.J. is a scientific advisor to AstraZeneca, Novartis, Genentech, AVRO Bio and Foresite Labs, reports speaking fees from GSK, is an equity holder and on the scientific advisory board for Bitterroot Bio, and is an equity holder, co-founder and on the scientific advisory board of TenSixteen Bio. The other authors declare no competing interests.

Additional information

Extended data is available for this paper at <https://doi.org/10.1038/s44161-023-00326-7>.

Supplementary information The online version contains supplementary material available at <https://doi.org/10.1038/s44161-023-00326-7>.

Correspondence and requests for materials should be addressed to Philipp J. Rauch or Siddhartha Jaiswal.

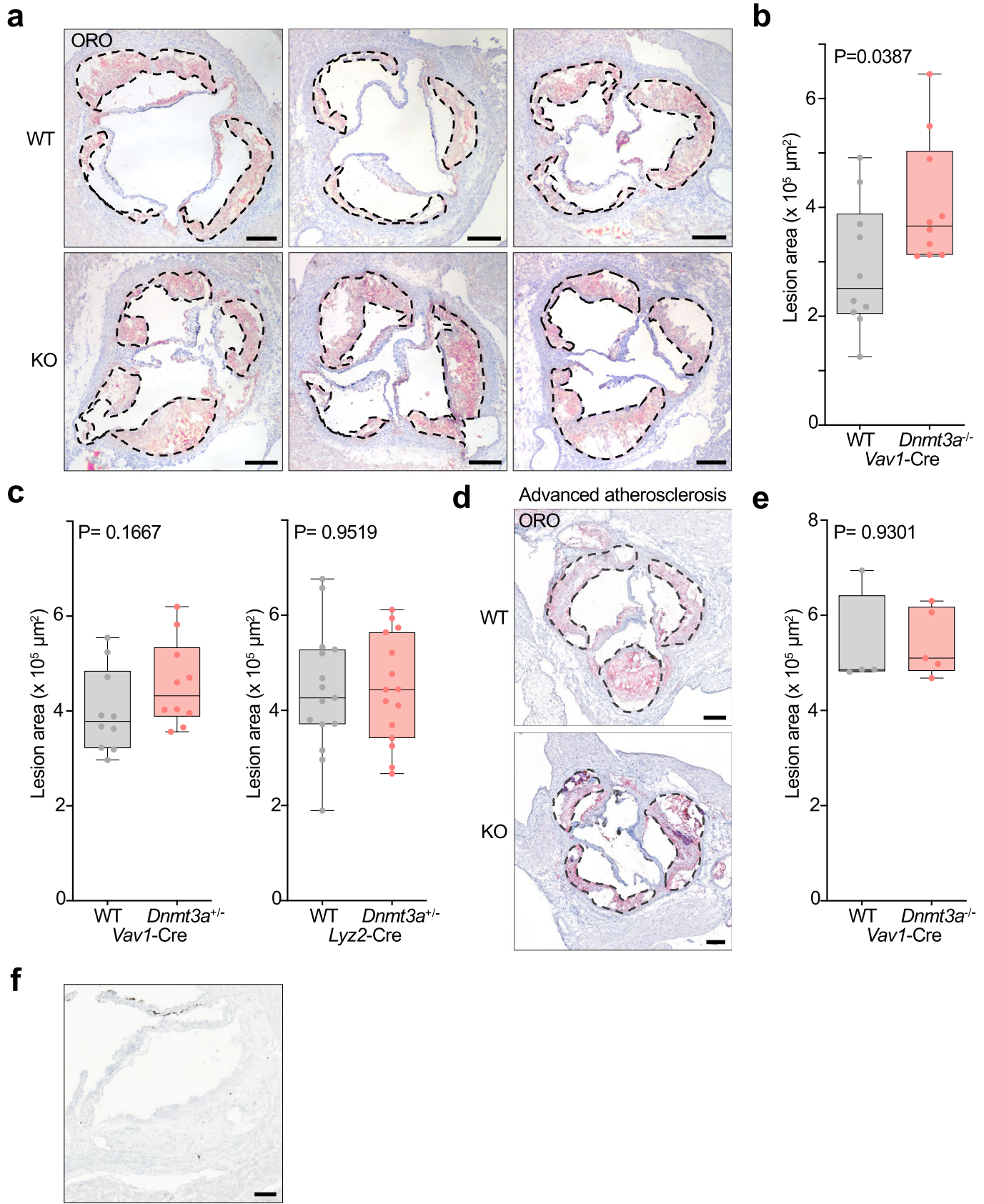
Peer review information *Nature Cardiovascular Research* thanks Franco Izzo, Alan Tall and the other, anonymous, reviewer(s) for their contribution to the peer review of this work.

Reprints and permissions information is available at www.nature.com/reprints.

Publisher's note Springer Nature remains neutral with regard to jurisdictional claims in published maps and institutional affiliations.

Springer Nature or its licensor (e.g. a society or other partner) holds exclusive rights to this article under a publishing agreement with the author(s) or other rightsholder(s); author self-archiving of the accepted manuscript version of this article is solely governed by the terms of such publishing agreement and applicable law.

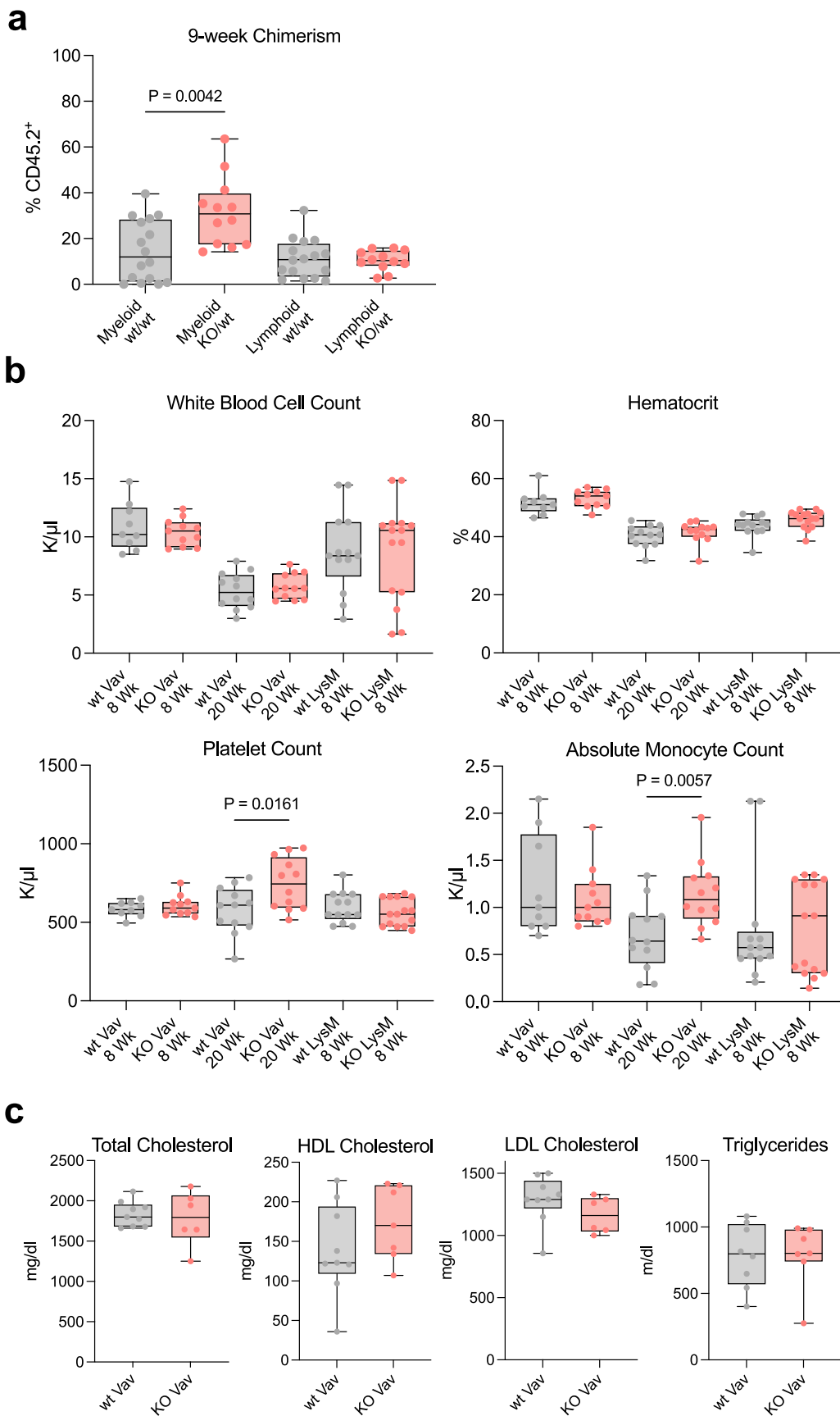
© The Author(s), under exclusive licence to Springer Nature Limited 2023



Extended Data Fig. 1 | See next page for caption.

Extended Data Fig. 1 | Extended phenotypic characterization of *Dnmt3a* loss impacting atherosclerosis. **a–b,** Bi-allelic loss of *Dnmt3a* in hematopoietic cells accelerates atherosclerosis. **(a)** Oil red O (ORO) stained aortic root sections in female *Ldlr^{-/-}* mice transplanted with either *Dnmt3a^{+/+}*; *Vav1-Cre* (WT) or *Dnmt3a^{-/-}*; *Vav1-Cre* (KO) marrow, in a 1:9 ratio with WT, after 9 weeks of feeding on high-fat, high-cholesterol diet. Atheromata are demarcated by dashed lines. Scale bars = 200 µm. **(b)** Quantification of lesion area in the aortic root. N = 10 animals for both groups. Unpaired two-tailed t-test with Welsh's correction. Box plot shows min, 25th percentile, median, 75th percentile and max. **c,** Single-allele loss of *Dnmt3a* has minimal impact on atherosclerosis. Shown is lesion area after 9 weeks on diet in female *Ldlr^{-/-}* mice that were transplanted with either *Dnmt3a +/−*; *Vav1-Cre* marrow (left) or *Dnmt3a +/−*; *Lyz2-Cre* marrow (right), compared to WT controls. N = 10 animals per group for *Vav1-Cre* experiment,

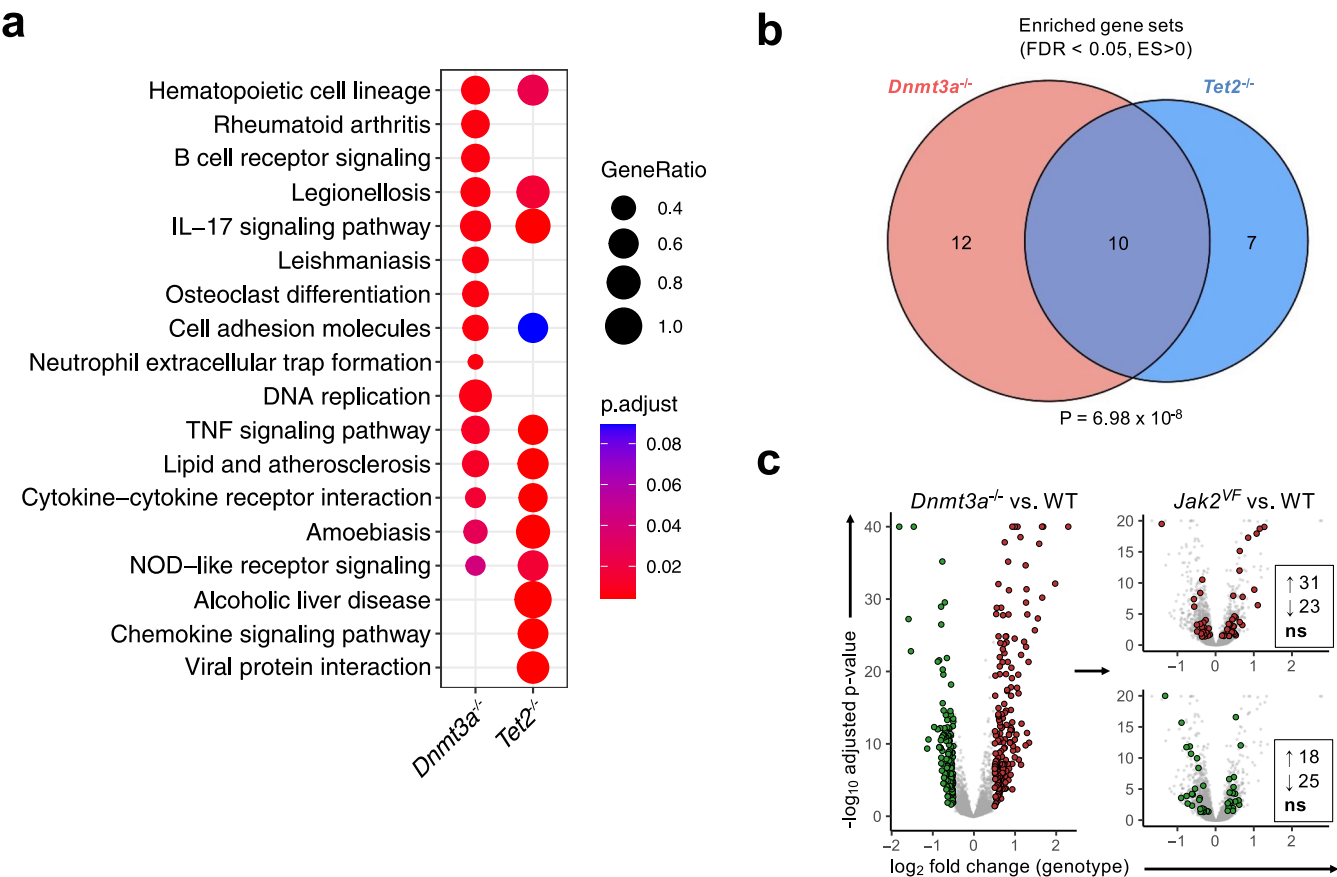
N = 15 per group for *Lyz2-Cre* experiment. Unpaired two-tailed t-test with Welch's correction. Box plots show min, 25th percentile, median, 75th percentile and max. **d–e,** Lesion size in advanced atherosclerosis does not differ between WT and *Dnmt3a* knock-out. **(d)** ORO-stained aortic root sections in female *Ldlr^{-/-}* mice transplanted with either *Dnmt3a^{+/+}*; *Vav1-Cre* (WT) or *Dnmt3a^{-/-}*; *Vav1-Cre* (KO) marrow, after 20 weeks of feeding on high-fat, high-cholesterol diet. Atheromata are demarcated by dashed lines. Scale bars = 200 µm. **(e)** Quantification of lesional area in the aortic root. N = 4 mice for WT and N = 5 for KO group. Unpaired two-tailed t-test with Welsh's correction. Box plot shows min, 25th percentile, median, 75th percentile and max. **f,** Isotype control (rabbit IgG) IHC staining for CD68 on aortic root with atheroma (control for Fig. 1c–d) demonstrates specificity of staining. Scale bar = 100 µm.



Extended Data Fig. 2 | See next page for caption.

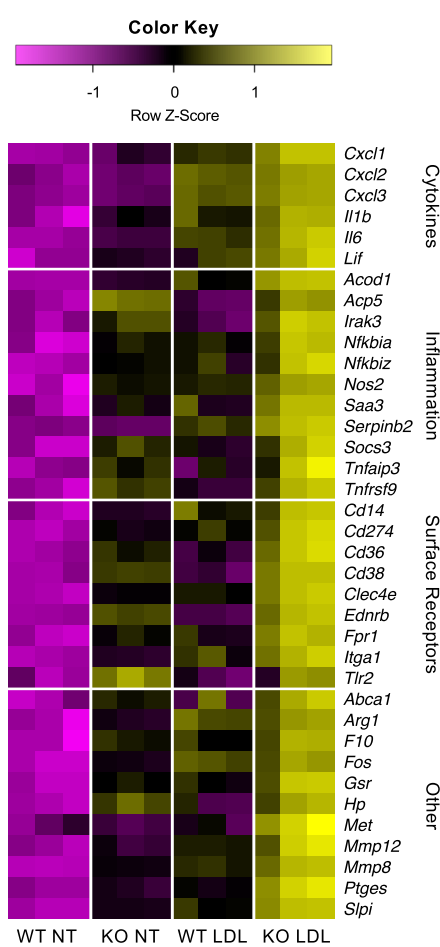
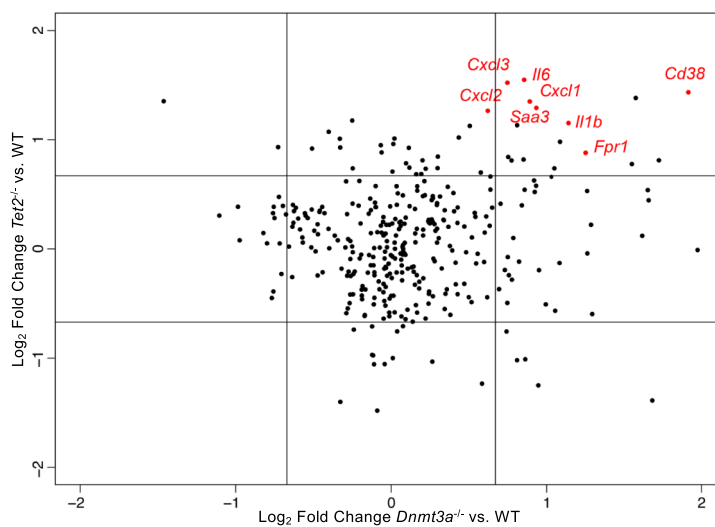
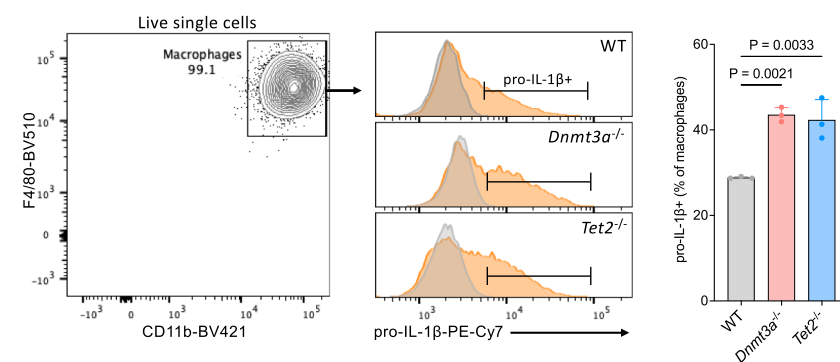
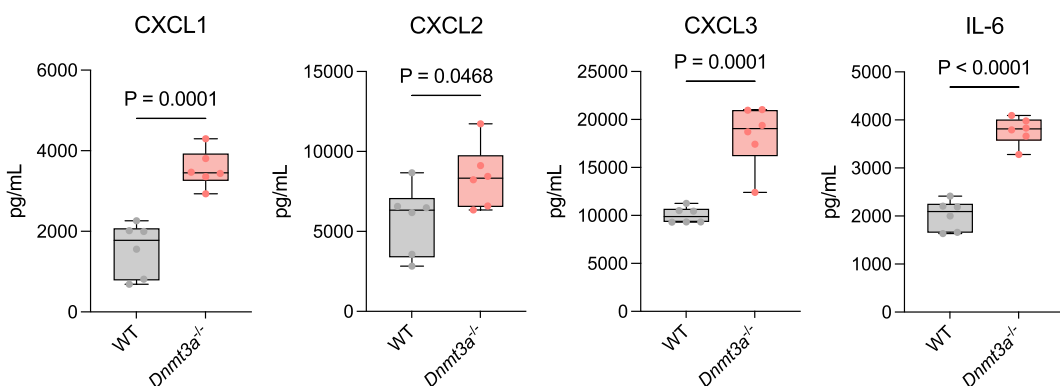
Extended Data Fig. 2 | Peripheral blood counts, chimerism and serum lipids in mice transplanted with *Dnmt3a*-deficient marrow. **a**, Peripheral blood chimerism in mice transplanted with either CD45.2⁺ *Vav1*-Cre (wt) or CD45.2⁺ *Dnmt3a*^{−/−}; *Vav1*-Cre (KO) marrow, in a 1:9 ratio with CD45.1⁺ WT, after 9 weeks on diet. N = 16 animals for WT group and N = 12 animals for KO group. Two-tailed unpaired t test was performed to compare the myeloid cell population between groups. **b**, Peripheral blood cell counts in transplanted mice. Indicated are transplanted genotypes and time on high-fat, high-cholesterol diet. Groups that received only wild-type marrow are marked in gray, and groups that received

marrow with bi-allelic loss of *Dnmt3a* are marked in red. N = 9 for wt Vav 8 Wk, N = 11 for KO Vav 8 Wk, N = 12 for wt Vav 20 Wk and KO Vav 20 Wk, N = 13 for wt LysM 8 Wk, N = 15 for KO LysM 8 Wk. P values obtained by two-tailed unpaired t tests. **c**, Serum lipid concentrations in mice transplanted with either *Vav1*-Cre (wt) or CD45.2⁺ *Dnmt3a*^{−/−}; *Vav1*-Cre (KO) marrow, after 14 weeks on diet. For total cholesterol, N = 9 for wt, N = 6 for KO. For HDL, N = 9 for wt, N = 7 for KO. For LDL, N = 9 for wt, N = 6 for KO. For triglycerides, N = 8 for wt, N = 7 for KO. Varying group sizes due to insufficient volume for all analyses in some samples. All box plots show min, 25th percentile, median, 75th percentile and max.


Extended Data Fig. 3 | Comparative gene-set enrichment analysis.

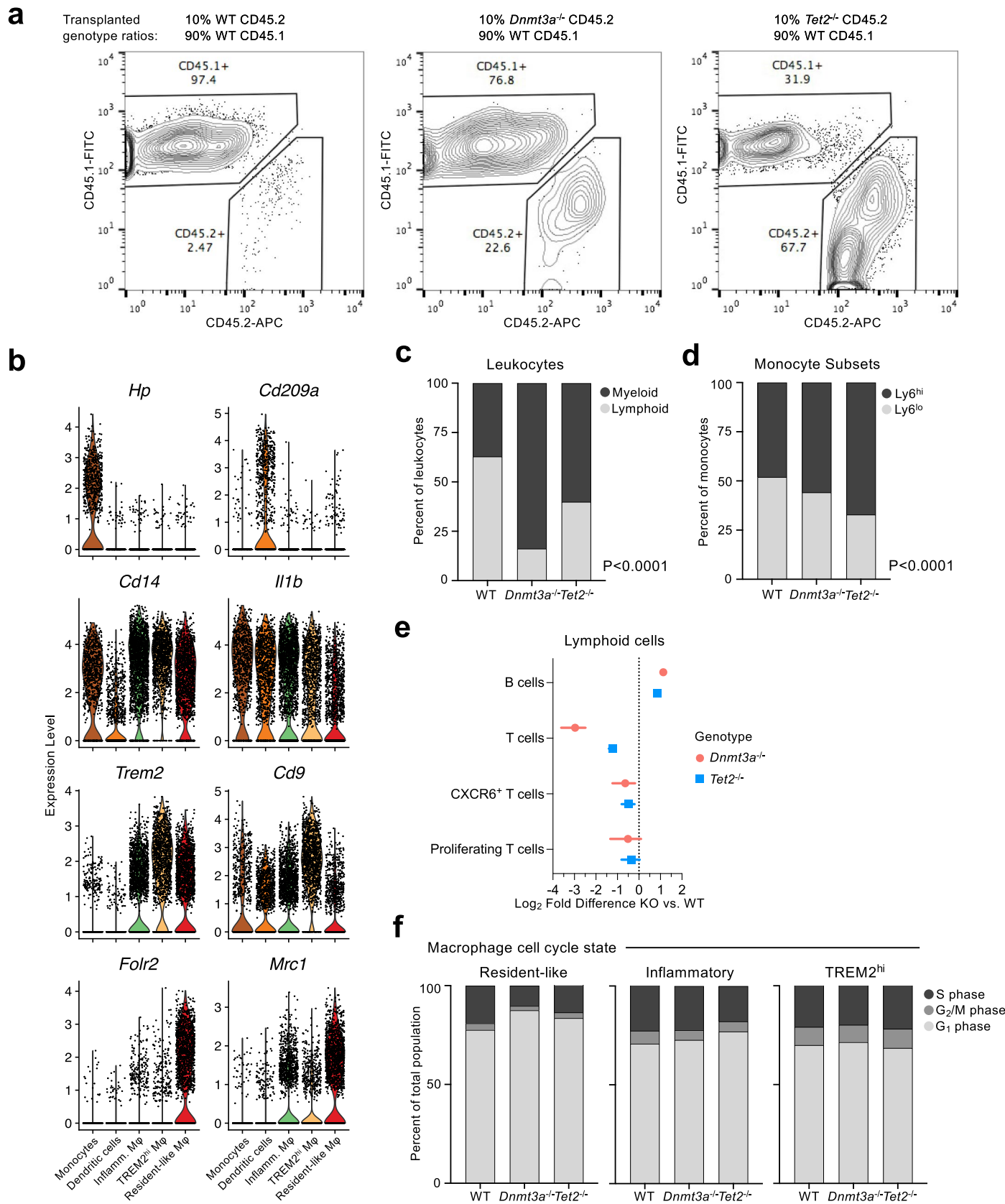
a, Comparative GSEA using the merge_result function in clusterProfiler between *Dnmt3a*^{-/-} and *Tet2*^{-/-}; *Vav1*-Cre BMDM. Top enriched KEGG pathways in *Dnmt3a*^{-/-} and *Tet2*^{-/-} (showCategory = 10) are shown. P value estimation in the fgsea method used by clusterProfiler is based on an adaptive multi-level split Monte-Carlo scheme. Adjustment for multiple comparisons was performed using the Benjamini-Hochberg method. **b**, Venn diagram showing overlap in the identity of significantly enriched (FDR < 0.05, ES > 0) 2019 KEGG pathways obtained by gene-set enrichment analysis (GSEA) in *Dnmt3a*^{-/-} vs. WT (red) or

Tet2^{-/-} vs. WT (blue) BMDM, see Supplementary Table for detailed listing of all enriched pathways. Statistical significance calculated by the hypergeometric test. **c**, Specificity test of enriched gene distribution analysis using *Jak2*^{VF} as a comparator. Enriched (\log_2 FC > 0.5 and $p < 0.05$, red dots) or depleted (\log_2 FC < -0.5 and $p < 0.05$, green dots) transcripts in *Dnmt3a*^{-/-} BMDM were tested for enrichment or depletion ($p < 0.05$) in *Jak2*^{VF} BMDM. The resulting distribution for each permutation was statistically compared to an equipartition (boxes) by way of a two-sided Chi-square test.

a**b****c****d**

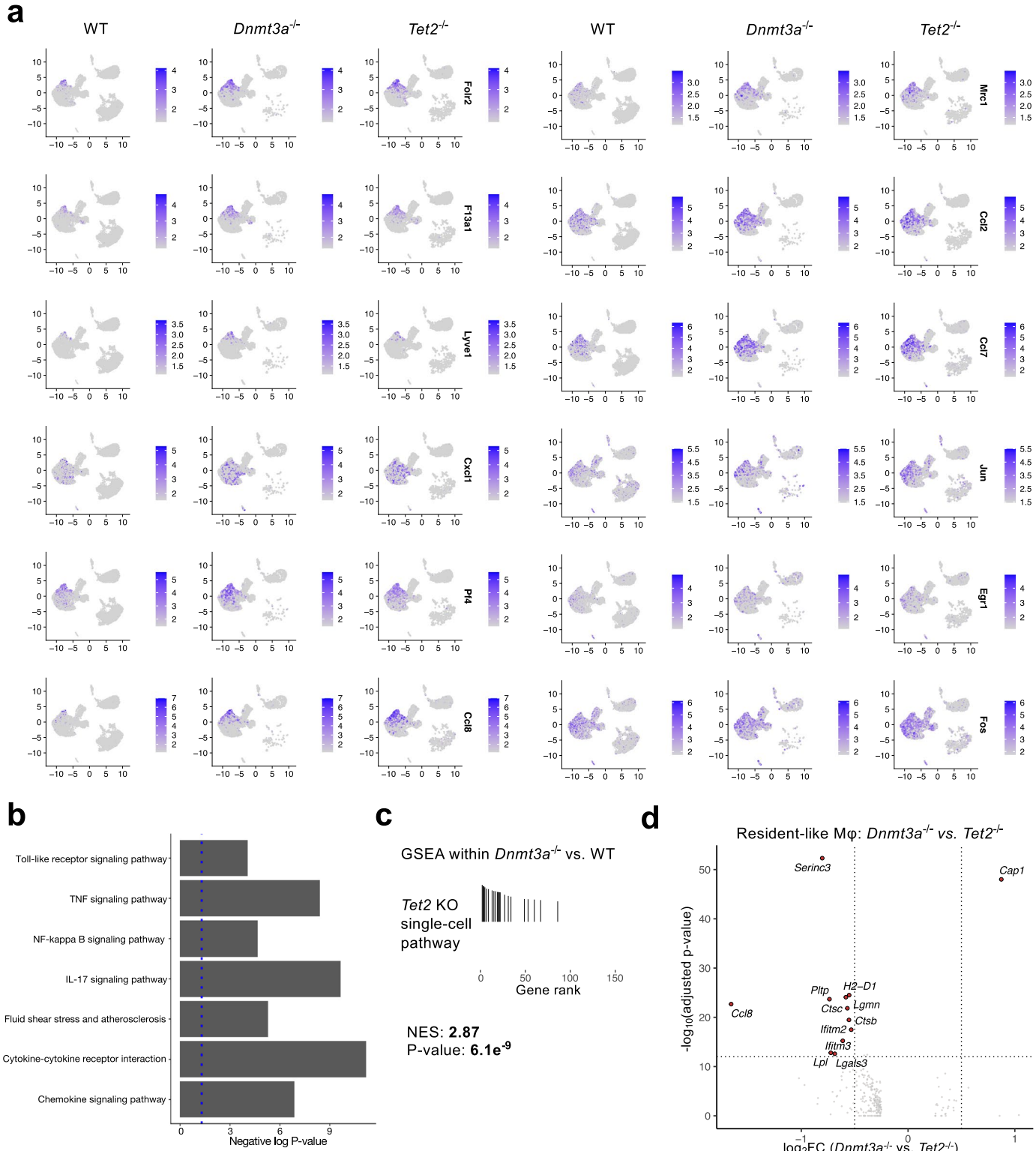
Extended Data Fig. 4 | Convergent changes in inflammatory pathways with *Dnmt3a* and *Tet2* deficiency. **a**, BMDM were cultured with LDL or vehicle (NT = non-treated) for 24 h, and mRNA was assessed by RNA-seq. Out of the top 200 genes that were affected by both LDL treatment and genotype ($\log_2\text{FC} > 0.6$, adjusted p -value < 0.05), 37 selected genes involved in inflammation are shown. Each column in the heatmap represent an individual biological replicate. **b**, Scatter plot comparing gene expression changes in *Dnmt3a*^{-/-} vs. WT with the *Tet2*^{-/-} vs. WT dataset from Jaiswal et al., 2017. Displayed are the most highly expressed genes significantly affected by 200 mg/dL LDL stimulation in BMDM. Red dots highlight genes involved in chemokine signaling. Shown are mean fold changes over 3 biological replicates per genotype and stimulation status for the WT vs *Dnmt3a*^{-/-} comparison; for the WT vs *Tet2*^{-/-} comparison, 3 biological replicates per genotype for the non-treated condition and 2 replicates for the LDL condition. **c**, Intracellular flow cytometry validates increase in pro-IL-1 β in stimulated *Dnmt3a*^{-/-} and *Tet2*^{-/-} BMDM vs. WT at the protein level. Flow cytometry plot depicts macrophage gating strategy (showing WT as a representative example). Histograms show unstimulated BMDM (gray) overlaid onto stimulated BMDM (orange). Bar graph shows quantification. $N = 3$ per group, mean \pm SD. P values obtained by one-way ANOVA followed by Tukey's post hoc test. **d**, ELISA for key secreted cytokines measured in supernatant of LDL-stimulated BMDM from WT or *Dnmt3a*^{-/-}. $N = 6$ per group (biological replicates). Two-tailed unpaired t-tests. Box plots show min, 25th percentile, median, 75th percentile and max.

comparison, 3 biological replicates per genotype for the non-treated condition and 2 replicates for the LDL condition. **c**, Intracellular flow cytometry validates increase in pro-IL-1 β in stimulated *Dnmt3a*^{-/-} and *Tet2*^{-/-} BMDM vs. WT at the protein level. Flow cytometry plot depicts macrophage gating strategy (showing WT as a representative example). Histograms show unstimulated BMDM (gray) overlaid onto stimulated BMDM (orange). Bar graph shows quantification. $N = 3$ per group, mean \pm SD. P values obtained by one-way ANOVA followed by Tukey's post hoc test. **d**, ELISA for key secreted cytokines measured in supernatant of LDL-stimulated BMDM from WT or *Dnmt3a*^{-/-}. $N = 6$ per group (biological replicates). Two-tailed unpaired t-tests. Box plots show min, 25th percentile, median, 75th percentile and max.



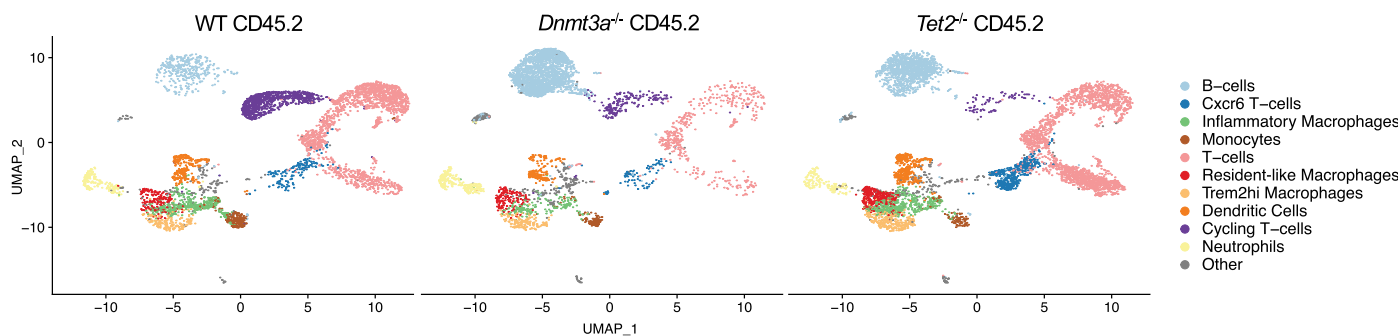
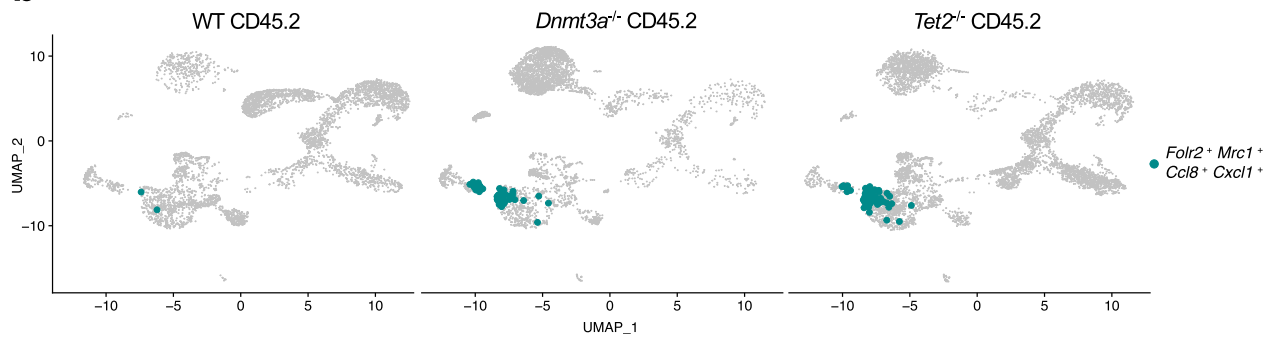
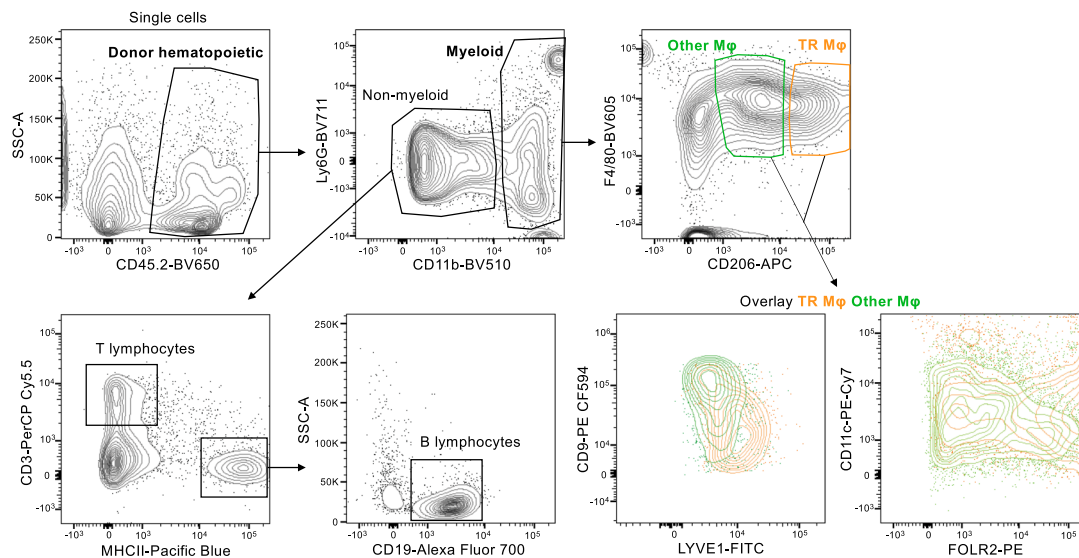
Extended Data Fig. 5 | Single-cell RNA sequencing (scRNA-seq) from atheromata. **a**, Flow cytometric analysis of chimerism in aortic single cell suspensions from mixed chimeric *Ldlr*^{-/-} mice on 30 weeks of high fat, high cholesterol diet. Transplanted genotypes and ratios are indicated. Dot plots show live, doublet excluded, CD45 positive cells. **b**, Violin plots depict single-cell expression of key signature genes across the 5 classic mononuclear phagocyte populations. Color code follows Fig. 3b. **c-e**, Lesional cell distribution is shaped

by genotype. **(c)** Major leukocyte lineages. Chi square test. **(d)** Monocyte subsets. Chi square test. **(e)** Proportions-of-clusters analysis within the lesional lymphocyte compartment. Displayed is \log_2 fold difference and 95% confidence interval. Permutation test with $N = 1000$ permutations. Full statistics are reported in Supplementary Table 3. **f**, Single-cell transcriptome-based cell cycle analysis in macrophages stratified by subset and genotype.



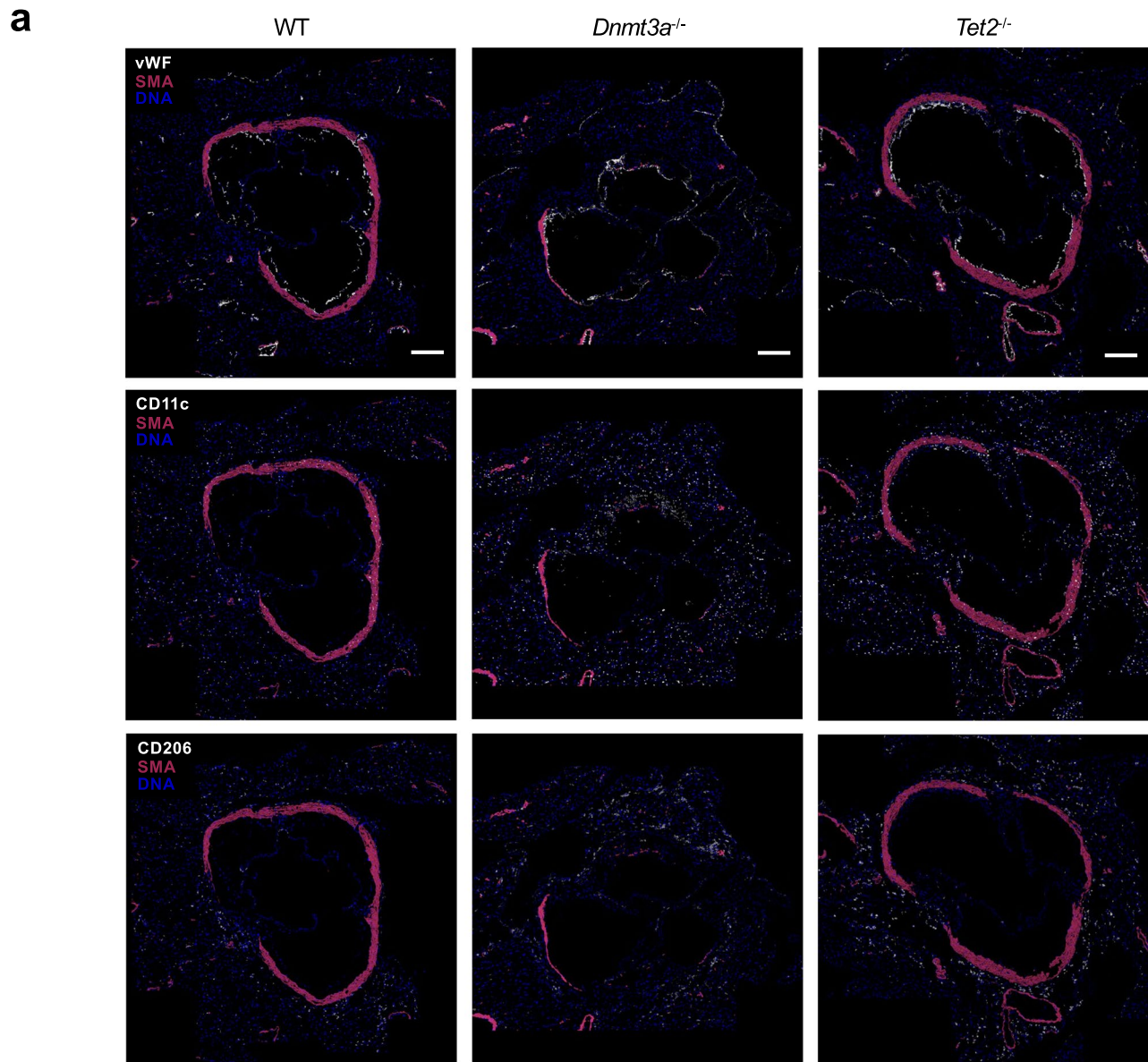
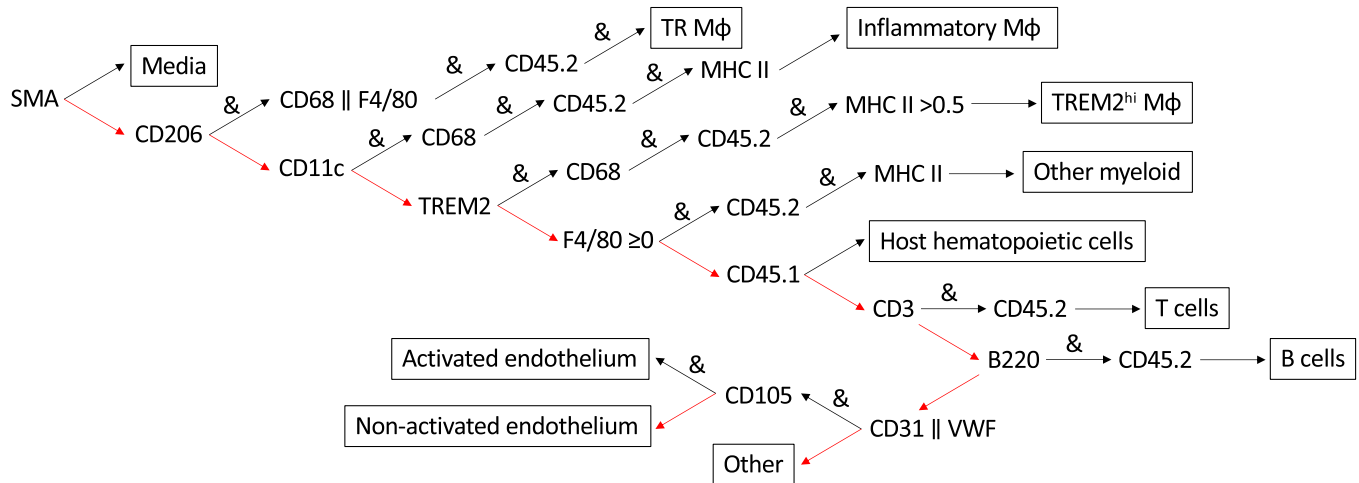
Extended Data Fig. 6 | CHIP gives rise to a distinct macrophage population in atheromata. **a**, UMAP plot of highly expressed genes that are differentially upregulated in the *Folr2*⁺ *Mrc1*⁺ *Ccl8*⁺ *Cxcl1*⁺ macrophage cluster separated by genotype (WT, *Dnmt3a*^{-/-}; *Vav1-Cre*, and *Tet2*^{-/-}; *Vav1-Cre*). **b**, Significantly enriched 2019 Kyoto Encyclopedia of Genes and Genomes (KEGG) pathways involved in inflammation and aging in the CHIP-TR macrophage population, analogous to the analysis in BMDM depicted in Fig. 2. Tested genes were present in at least 25% of the CHIP-TR macrophage subpopulation with a positive log fold change of at least 0.25. Dotted blue line indicates P value of 0.05. P values were calculated by Fisher's exact test using the R package enrichr. **c**, GSEA of a pathway

comprising the top 25 upregulated genes in *Tet2*^{-/-} vs. WT by $\log_2\text{FC}$ within the Resident-like M ϕ cluster ('*Tet2* KO sc-pathway') within the *Dnmt3a*^{-/-} vs. WT ranking in the same cluster, analogous to the BMDM analysis in Fig. 2d. P value estimation in the fgsea method is based on an adaptive multi-level split Monte-Carlo scheme. **d**, Volcano plot depicts differential gene expression analysis in *Dnmt3a*^{-/-} vs. *Tet2*^{-/-} within the resident-like macrophage (M ϕ) cluster using the FindMarkers function in Seurat ($\text{logfc.threshold} = 0.25$) using a negative binomial generalized linear model. Labeled are genes with a $|\log_2\text{FC}| > 0.5$ (vertical lines) and adjusted p-value $< 10^{-12}$ (horizontal line).

a**b****c**

Extended Data Fig. 7 | Expansion of *Folr2⁺ Mrc1⁺ Ccl8⁺ Cxcl1⁺* macrophages in CHIP. **a**, UMAP plots of aligned gene expression data in single CD45.2⁺ cells isolated from aortae from WT; *Vav1-Cre* (n = 5015), *Dnmt3a^{-/-}; Vav1-Cre* (n = 4499), and *Tet2^{-/-}; Vav1-Cre* (n = 6078) populations (24-week cohort). **b**, *Folr2⁺ Mrc1⁺ Ccl8⁺ Cxcl1⁺* (CHIP-TR) macrophages highlighted on the UMAP plots from **a** following 24 weeks of high-fat, high-cholesterol diet. Gray dots

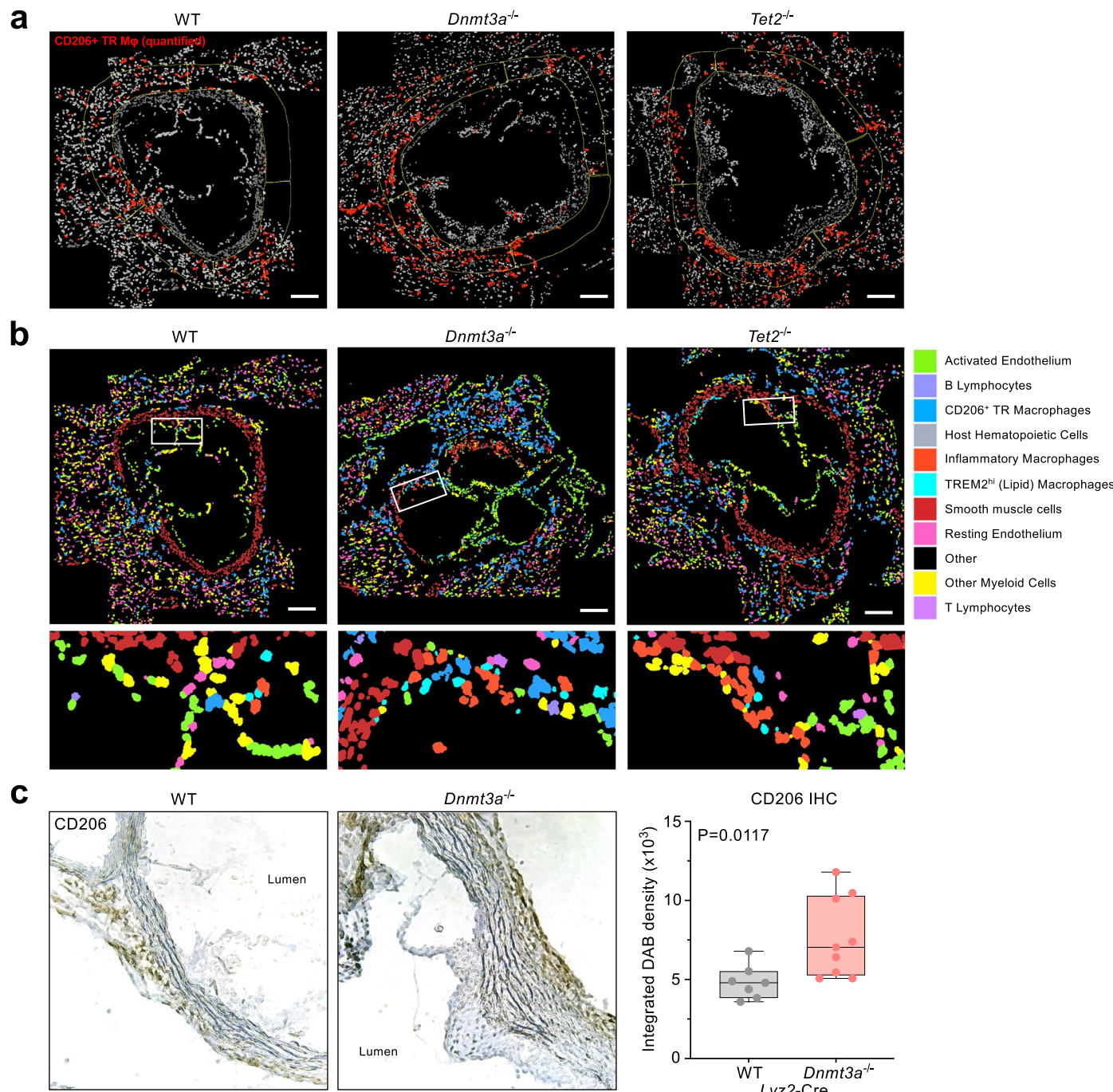
correspond to all other cells. Quantification in Fig. 4d. **c**, Gating strategy for identification of donor-derived tissue resident-like (TR) macrophages in atherosoma by flow cytometry. The population was defined as CD45.2⁺ CD11b⁺ F4/80⁺ CD206^{hi/+}. Comparison to other macrophages (CD206^{lo}) confirmed higher expression of LYVE1 and FOLR2, and lower expression of CD9, as expected from scRNA-seq.

**b**

Extended Data Fig. 8 | See next page for caption.

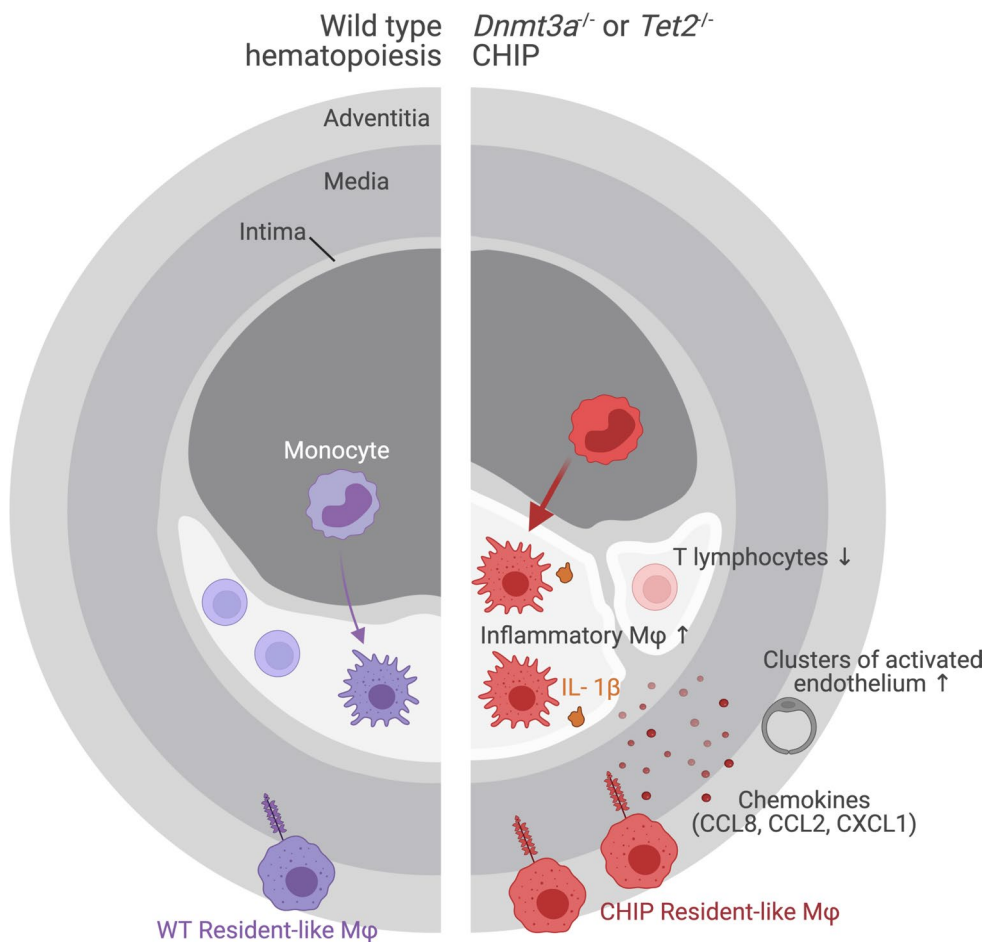
Extended Data Fig. 8 | Multiplex Ion Beam Imaging by Time-of-Flight (MIBI-TOF) of aortic roots in WT, *Dnmt3a*^{-/-} and *Tet2*^{-/-}. **a.** MIBI-TOF of aortic roots in WT, *Dnmt3a*^{-/-} and *Tet2*^{-/-}. Shown are 3 exemplary antigens (in white) with relevance to atherosclerosis (von Willebrand factor [VWF], integrin subunit alpha X/CD11c and mannose receptor 1/CD206) out of 27 total markers recorded. DNA (blue) and SMA (magenta) channels are shown to provide anatomical reference.

Scale bars = 200 μ m. **b.** Biologically informed decision tree used to define cell identities (boxes) based on combinations of antigen markers. Black arrows signify condition fulfilled/marker positive. Red arrows signify that the preceding (combination of) condition(s) has not been fulfilled. & = AND. || = OR. TR M Φ = tissue resident-like macrophage.



Extended Data Fig. 9 | CHIP alters the spatial cellular composition of atheromata. **a**, Quantification strategy for adventitial CD206⁺ TR macrophages in 5-week roots (N = 9). For each section (biological replicate), the average of 4 ROIs was reported (demarcated by yellow lines). Scale bars = 200 μ m. **b**, Section of the arterial intima (white rectangles), high-power images below, depicting

nascent atheromata (scale bars = 200 μ m). **c**, IHC for CD206 on aortic roots in WT and *Dnmt3a*^{-/-} mice. Graph shows quantification of 3,3'-Diaminobenzidine (DAB) density, normalized to (arc) length of the section measured. N = 7 mice per WT and N = 9 mice for KO group. Unpaired two-tailed t-test with Welch's correction. Box plots show min, 25th percentile, median, 75th percentile and max.



Extended Data Fig. 10 | Summary. Mutations in the epigenetic regulators *Dnmt3a* or *Tet2* in hematopoietic cells converge in the emergence of a distinct macrophage subset in the arterial adventitia (denoted CHIP Resident-like Mφ) that combines surface markers associated with resident-like macrophages (depicted: mannose receptor/CD206) with a distinct inflammatory chemokine

signature. These cells are surrounded by other myeloid cells and clusters of activated endothelium. Overall, lesional (inflammatory) macrophage content increases, while other immune cell subsets, in particular T lymphocytes, decrease. Collectively, these processes result in increased atherosclerosis.

Reporting Summary

Nature Portfolio wishes to improve the reproducibility of the work that we publish. This form provides structure for consistency and transparency in reporting. For further information on Nature Portfolio policies, see our [Editorial Policies](#) and the [Editorial Policy Checklist](#).

Statistics

For all statistical analyses, confirm that the following items are present in the figure legend, table legend, main text, or Methods section.

n/a Confirmed

- The exact sample size (n) for each experimental group/condition, given as a discrete number and unit of measurement
- A statement on whether measurements were taken from distinct samples or whether the same sample was measured repeatedly
- The statistical test(s) used AND whether they are one- or two-sided
Only common tests should be described solely by name; describe more complex techniques in the Methods section.
- A description of all covariates tested
- A description of any assumptions or corrections, such as tests of normality and adjustment for multiple comparisons
- A full description of the statistical parameters including central tendency (e.g. means) or other basic estimates (e.g. regression coefficient) AND variation (e.g. standard deviation) or associated estimates of uncertainty (e.g. confidence intervals)
- For null hypothesis testing, the test statistic (e.g. F , t , r) with confidence intervals, effect sizes, degrees of freedom and P value noted
Give P values as exact values whenever suitable.
- For Bayesian analysis, information on the choice of priors and Markov chain Monte Carlo settings
- For hierarchical and complex designs, identification of the appropriate level for tests and full reporting of outcomes
- Estimates of effect sizes (e.g. Cohen's d , Pearson's r), indicating how they were calculated

Our web collection on [statistics for biologists](#) contains articles on many of the points above.

Software and code

Policy information about [availability of computer code](#)

Data collection	Flow cytometry data was collected using FACS DIVA version 8.0.1 or earlier (BD Pharmingen) and analyzed using FlowJo 10.8.2. Sequencing data was collected on the NextSeq500, or HiSeq2500 Systems (Illumina).
Data analysis	<p>RNA sequencing: Reads were mapped to the <i>Mus musculus</i> mm10 reference genome with the CLC Genomics Server program v. 9.0.1. RNaseq Normalized read counts were obtained from the resulting BAM files using the BiocLite (https://bioconductor.org/biocLite.R) package in R version 3.17 or earlier. Differential gene expression was analyzed using the Deseq2 (https://bioconductor.org/packages/release/bioc/html/DESeq2.html) package in R considering the effect of LDL treatment and genotype as separate variables in a linear model (design = ~ genotype + treatment). Genes were assigned p-values based on being differentially expressed due to genotype, and separate p-values were obtained for differential expression based on treatment. Genes with $q < 0.05$ were considered significant in each respective analysis. Gene Set Enrichment Analysis was performed using the Broad GSEA pipeline and the R packages clusterProfiler version 4.8.1 or earlier, Enrichr and fgsea version 1.26.0 or earlier.</p> <p>scRNA-seq: The BCL files were demultiplexed using 8 base-pair 10X sample indexes and “cellranger mkfastq” to generate paired-end FASTQ. We ran “cellranger count” to align the reads to the mouse UCSC mm10 reference genome using STAR aligner as well as perform filtering, barcode counting, and UMI counting. The alignment results were used to quantify the expression level of mouse genes and generation of gene-barcode matrix. Each sample’s cellranger matrix was then loaded in a SeuratObject_4.1.0 using Seurat_4.1.1 (https://github.com/satijalab/seurat). The R code used for further analysis is available on GitHub, and summarized below.</p> <p>QC and filtering parameters. Low quality cells, doublets, and potential dead cells were removed according to the percentage of mitochondrial genes and number of genes expressed in each cell (nFeature_RNA > 200 & nFeature_RNA < 4400 & percent.mt < 15). Filtering parameters were based on visualized QC metrics using the percent.mt/nCount_RNA and nFeature_RNA/nCount_RNA plots.</p> <p>Normalization, variable feature selection, scaling and linear dimensionality reduction. Samples were then normalized using a global-scaling</p>

normalization method called Log Normalize. Using the FindVariableFeatures function, the top 2000 most highly variable genes were identified and used for downstream analysis to highlight biological signal. Cell cycle scores were assigned using Seurat's CellCycleScoring function. Linear transformation scaling was performed to prepare the data for dimensional reduction techniques. Cell cycle scores were regressed out during data scaling, followed by principal component analysis.

Integration and clustering. The different objects were then integrated using Harmony (<https://github.com/immunogenomics/harmony>). Based on the ElbowPlot, we selected 8 significant dimensions to cluster the cells. Dimensionality reduction via UMAP embedding was performed on the integrated dataset, followed by the FindNeighbors and FindClusters functions.

Doublet detection. Doublet detection and removal was performed on the 30-week dataset using doubletFinder_v3 (<https://github.com/chris-mcginnis-ucsf/DoubletFinder>).

Downstream analysis and data visualization. Identities of the cell clusters were determined using canonical cell type markers. For identification of cluster signature genes, we used the FindAllMarkers function in the Seurat package using the Wilcoxon Rank Sum test, testing genes that were detected in at least 25% of cells in either of the two groups with at least a 0.25 difference (log-scale) between the two groups, and at least 3 cells expressing the feature in at least one of the two groups. Differential gene expression within the Resident-like macrophage cluster was calculated using the FindMarkers function, using a negative binomial generalized linear model. We tested genes that were detected in at least 10% of cells in WT or mutant populations, with at least a 0.25 difference (log-scale) between the two groups of cells, and at least 3 cells expressing the feature in at least one of the two groups. The difference between the proportion of celltypes across different samples was calculated by a proportion test using the Single Cell Proportion Test R package (<https://github.com/rpolicastro/scProportionTest>).

Analysis of the 24-week dataset. For the 24-week dataset, an analogous analysis was performed with three modifications: (1) filtering parameters were nFeature_RNA > 300 & nFeature_RNA < 4500 & percent.mt < 15, again based on visualizing QC metrics; (2) we used sctransform-based normalization; (3) we selected 11 dimensions to cluster the cells, again based on the ElbowPlot.

MIBI Analysis: For each field of view, Mass-spec pixel data were converted to a multi-dimensional TIFF. Counts for each mass were defined according to whether they fell between the 'Start' and 'Stop' values defined in table S1. Background across all channels was highly correlated to bare spots (with no tissue) on the slide. Background was filtered using a blank channel (mass 128-132). The background image was smoothed using a Gaussian kernel and then thresholded to obtain a binary mask. Following the subtraction, negative values were converted to zeros. We found that this removal was sufficient to remove background-related noise, while preserving real signal. To filter noise by signal density a k-nearest-neighbor approach was used. Each count was given a density-determined confidence score, by calculating the average distance to the 25 nearest positive counts. Pixels with counts larger than one were treated as several counts with distance 0 from each other. Removal thresholds were determined as the crossing points in the bimodal distributions and low-confidence counts were removed. In addition to the real staining, some channels exhibited dense, localized staining, which appeared like 'antibody aggregates'. To remove aggregates, denoised images were smoothed using a Gaussian kernel with R = 1 and the resulting image was binarized using Otsu's method. Pixels of small connected components were set to zero.

Downstream density analyses were carried out in ImageJ/FIJI version 2.3.0/1.53t.

For manuscripts utilizing custom algorithms or software that are central to the research but not yet described in published literature, software must be made available to editors and reviewers. We strongly encourage code deposition in a community repository (e.g. GitHub). See the Nature Portfolio [guidelines for submitting code & software](#) for further information.

Data

Policy information about [availability of data](#)

All manuscripts must include a [data availability statement](#). This statement should provide the following information, where applicable:

- Accession codes, unique identifiers, or web links for publicly available datasets
- A description of any restrictions on data availability
- For clinical datasets or third party data, please ensure that the statement adheres to our [policy](#)

The data supporting the findings of this study are available within the paper and its supplementary information and source files. All sequencing data from this study has been deposited in the National Center for Biotechnology Information Gene Expression Omnibus (GEO accession numbers GSE225773 for scRNA-seq and GSE237599 for bulk RNA-seq). The UCSC mm10 reference genome was used for alignment of sequencing data. Multiplexed imaging data has been deposited in Mendeley (<https://data.mendeley.com/datasets/dgyrt473vs/1>).

Human research participants

Policy information about [studies involving human research participants and Sex and Gender in Research](#).

Reporting on sex and gender

There were no human research participants involved in this study.

Population characteristics

There were no human research participants involved in this study.

Recruitment

There were no human research participants involved in this study.

Ethics oversight

There were no human research participants involved in this study.

Note that full information on the approval of the study protocol must also be provided in the manuscript.

Field-specific reporting

Please select the one below that is the best fit for your research. If you are not sure, read the appropriate sections before making your selection.

Life sciences

Behavioural & social sciences

Ecological, evolutionary & environmental sciences

For a reference copy of the document with all sections, see nature.com/documents/nr-reporting-summary-flat.pdf

Life sciences study design

All studies must disclose on these points even when the disclosure is negative.

Sample size	Sample size for mouse experiments was designed to be sufficient to detect a 40% difference in atherosclerotic lesion size at 9 weeks (the delta observed in Jaiswal et al. NEJM 2017) with 80% power at a type I error rate of 0.05.
Data exclusions	No data were excluded from analysis.
Replication	In vivo studies typically had an N>10 per group, sufficient to perform statistical comparison. The plaque size phenotype seen with Vav-Cre was replicated using Lyz2-Cre with similar results. Other key experiments, including single-cell RNA-seq and flow cytometry, were repeated at least once with similar results. MIBI experiments were done on two types of samples (5 wk roots, 17 wk arches) with similar results.
Randomization	Age- and sex-matched mice were randomly allocated to different groups for transplant experiments (usually by cage).
Blinding	Investigators measuring atherosclerotic lesion size were blinded to the genotype of the samples at time of analysis. Blinding was considered not feasible during data collection, and the procedures of harvesting, sectioning, staining and imaging aortic roots were not expected to be sensitive to bias.

Reporting for specific materials, systems and methods

We require information from authors about some types of materials, experimental systems and methods used in many studies. Here, indicate whether each material, system or method listed is relevant to your study. If you are not sure if a list item applies to your research, read the appropriate section before selecting a response.

Materials & experimental systems		Methods	
n/a	Involved in the study	n/a	Involved in the study
<input type="checkbox"/>	<input checked="" type="checkbox"/> Antibodies	<input checked="" type="checkbox"/>	<input type="checkbox"/> ChIP-seq
<input checked="" type="checkbox"/>	<input type="checkbox"/> Eukaryotic cell lines	<input type="checkbox"/>	<input checked="" type="checkbox"/> Flow cytometry
<input checked="" type="checkbox"/>	<input type="checkbox"/> Palaeontology and archaeology	<input checked="" type="checkbox"/>	<input type="checkbox"/> MRI-based neuroimaging
<input type="checkbox"/>	<input checked="" type="checkbox"/> Animals and other organisms		
<input checked="" type="checkbox"/>	<input type="checkbox"/> Clinical data		
<input checked="" type="checkbox"/>	<input type="checkbox"/> Dual use research of concern		

Antibodies

Antibodies used

For antibodies used in flow cytometry, see "Flow Cytometry" section.

MIBI Antibodies

Metal conjugated primary antibodies were prepared as described previously (Bendall et al., 2011). Following labeling, antibodies were diluted in Candor PBS Antibody Stabilization solution (Candor Bioscience GmbH, Wangen, Germany) to 0.2 mg mL⁻¹ and stored long-term at 4°C.

Antibody Target Provider Catalog Number Clone Element Mass Channel Titer (ug/mL)

CD31 Biolegend 102501 MEC13.3 IgG1 13.33

CD45.2 Biolegend 109802 104 IgG1 115 4.44

CD11c Biolegend 117302 N418 IgG1 142 4.00

CD115 Fluidigm 3144012B AFS98 IgG1 144 4.00

CD206 Biolegend 141701 C068C2 IgG1 145 2.00

F4/80 Biolegend 123102 BM8 IgG1 146 5.00

CD3 Biolegend 100202 17A2 IgG1 147 2.67

B220 ThermoFisher 14-0452-82 RA3-6B2 IgG1 149 4.00

Sarcomeric Actin Sigma A2172-2ML 5C5 IgG1 150 6.67

CCR2 R&D MAB55382 475303 IgG1 152 4.00

CD8 Biolegend 100702 53-6.7 IgG1 153 3.64

CD11b Novus Biologicals NB110-89474 Polyclonal IgG1 154 4.00

IL-1B GeneTex GTX74034 Polyclonal Gd 158 2.00
 CCL8 ThermoFisher PA5-81333 Polyclonal Tb 159 2.00
 Ly-6C Biolegend 128002 HK1.4 Dy 162 4.00
 VWF Abcam ab6994 Polyclonal Pr 163 4.00
 CD105 Biolegend 120401 MJ7/18 Dy 164 10.00
 Lyve1 Novus Biologicals NB100-725 Polyclonal Ho 165 4.00
 FcεRI Biolegend 134308 Mar-Er 166 2.67
 Collagen Abcam ab34710 Polyclonal Er 167 2.00
 CD68 Biolegend 137002 FA-11 Tm 169 5.00
 CD49b Biolegend 108910 DX5 Er 170 4.00
 CD4 Biolegend 100506 RM4-5 Yb 172 4.00
 MHCII Biolegend 107601 M5/114.15.2 Yb 174 5.00
 CD45.1 Biolegend 110702 A20 Yb 176 4.00
 TREM2 Novus Biologicals NBP1-22515 RM0139-5J46 Nd 148 4.00

2 hour Antibody Stain 2
 Antibody Target Provider Catalog Number Clone Element Mass Channel Titer (ug/mL)
 DNA Abcam ab27156 35I9 DNA Y 89 0.33
 SMA FisherScientific MAB1420 1A4 Nd 143 0.32

TREM2 validation secondary antibody
 Alexa Fluor 568 goat anti-rat IgG (H+L), Fisher Scientific, A11077, 1:1000

Validation

Validated MIBI antibodies using IHC/IF protocol: The protocol for IHC/IF closely followed the MIBI-TOF staining protocol, with a few changes. For IHC, before blocking, endogenous peroxidase activity was quenched by incubation in 3% H₂O₂ for 30 min and sections were washed with H₂O on orbital shaker for 5 min. Sections were stained using the ImmPRESS universal (Anti-Mouse/Anti-Rabbit) kit (Vector labs) according to the manufacturer's guidelines. For IF, the anti-TREM2 primary antibody was detected with a goat anti-rat Alexa Fluor 568-conjugated secondary antibody (ThermoFisher A-11077) at 1:1000. Weblinks to the validation details for individual antibodies can be found in Supplementary Figure 4.

Biolegend Validation (<https://www.biolegend.com/en-us/quality/product-development>): Clones of these hybridomas are carefully selected based on a number of criteria including robust growth and efficient production of a single clone of antibody that is specific to the intended target. The best clones move on to applications testing. Antibody clones are then tested in a variety of assays to see which applications they are suited for. As an example, clone 13A3-1 for phosphorylated STAT3 (Tyr705) demonstrated excellent performance in flow cytometry, western blot, and chromatin immunoprecipitation. Thus, the clone cross-validates itself by demonstrating functionality across orthogonal testing methods. Additionally, the biological induction of the phosphorylated state using IL-6 further validates the specificity of the antibody.

BD Biosciences Validation (<https://www.bdbiosciences.com/en-us/products/reagents/flow-cytometry-reagents/research-reagents/quality-and-reproducibility>): BD Biosciences identifies key targets of interest in scientific research and develops its own specific antibodies or collaborates with top research scientists around the world to license their antibodies. We then transform these antibodies into flow cytometry reagents by conjugating them to a broad portfolio of high-performing dyes, including our vastly popular portfolio of BD Horizon Brilliant™ Dyes. A world-class team of research scientists helps ensure that these reagents work reliably and consistently for flow cytometry applications. The specificity is confirmed using multiple methodologies that may include a combination of flow cytometry, immunofluorescence, immunohistochemistry or western blot to test staining on a combination of primary cells, cell lines or transfected models. All flow cytometry reagents are titrated on the relevant positive or negative cells. To save time and cell samples for researchers, test size reagents are bottled at an optimal concentration with the best signal-to-noise ratio on relevant models during the product development. To ensure consistent performance from lot-to-lot, each reagent is bottled to match the previous lot MFI. You can look up the Certificate of Analysis and the concentration of test-size human reagents from specific lots via the Concentration Lookup page or BD Regulatory Documents.

Technical data sheets provide data generated on the relevant primary model at this optimal concentration based on a titration curve. QC data on any lot of reagent can be requested through ResearchApplications@bd.com.

Animals and other research organisms

Policy information about [studies involving animals; ARRIVE guidelines](#) recommended for reporting animal research, and [Sex and Gender in Research](#)

Laboratory animals

Strains used in this study include the Dnmt3a-floxed line B6;129S-Dnmt3atm1.1Jae/J36, Tet2-floxed line B6;129S-Tet2tm1.1laai/J (Jax Cat. No. 017573)7, the hypercholesterolemia-prone Ldlr knockout (KO) line B6;129S7-Ldlrtm1Her/J (Jax Cat. No. 002207), and B6.SJL-Ptprca Pepcb/BoyJ (CD45.1+). Mice with constitutive expression of Cre recombinase under control of either the Vav1 promoter (B6.Cg-Tg(Vav1-cre)A2Kio/J [Jax Cat. No. 008610]) or LysM promoter (B6.129P2-Lyz2tm1(cre)Ifo/J [Jax Cat. No. 004781]) were crossed with the Dnmt3a- or Tet2-floxed line to generate animals with Dnmt3a or Tet2 KO specific to the entire hematopoietic or myeloid lineages, respectively. Where appropriate, wild-type Vav1-Cre or LysM-Cre animals were used as controls. Ldlr-/ mice were crossed with B6.SJL-Ptprca Pepcb/BoyJ (Jax Cat. No. 002014) to generate Ldlr-/ mice homozygous for the pan-leukocyte marker CD45.1. For transplant experiments, female CD45.1 Ldlr-/ mice were used exclusively as recipients. For transplantation (in vivo) experiments, animals were transplanted at 4 weeks of age and then analyzed between 5 and 30 weeks of age. For generation of BMMD, bone marrow was harvested from 10-14 week old animals. Housing conditions were characterized by a temperature of 70-74F and humidity between 30-70%.

Wild animals

Study did not include wild animals.

Reporting on sex

In line with NIH Guide Notice NOT-OD-15-102, both male and female mice were used in this study, as noted in individual experiments. Lesion size assessment was performed on female mice; this was done since we and others have observed less mouse-to-mouse variation in female animals.

Field-collected samples

Study did not include field-collected samples.

Ethics oversight

The Institutional Animal Care and Use Committees (IACUC) of Brigham and Women's Hospital (2017N000060) and Dana-Farber Cancer Institute (19-008) granted approval for all mouse experiments as described here.

Note that full information on the approval of the study protocol must also be provided in the manuscript.

Flow Cytometry

Plots

Confirm that:

- The axis labels state the marker and fluorochrome used (e.g. CD4-FITC).
- The axis scales are clearly visible. Include numbers along axes only for bottom left plot of group (a 'group' is an analysis of identical markers).
- All plots are contour plots with outliers or pseudocolor plots.
- A numerical value for number of cells or percentage (with statistics) is provided.

Methodology

Sample preparation

Aortic tissue (from the sinotubular junction to the bifurcation) was cut in small pieces and subjected to enzymatic digestion with 450 U/ml collagenase I, 125 U/ml collagenase XI, 60 U/ml DNase I and 60 U/ml hyaluronidase (Sigma-Aldrich, St. Louis, MO) for 1 h at 37 °C while shaking. The resulting cell suspension was passed through a 70 µm filter, followed by staining with the following monoclonal antibodies: Brilliant Violet 510 conjugated anti-CD11b (clone M1/70, BioLegend), Brilliant Violet 605 conjugated anti-F4/80 (clone BM8, BioLegend), Brilliant Violet 650 conjugated anti-CD45.2 (clone 104, BioLegend), Brilliant Violet 711 conjugated anti-Ly6G (clone 1A8, BD Biosciences), Brilliant Violet 786 conjugated anti-CD16/32 (clone 93, BD Biosciences), Alexa Fluor 488 conjugated anti-Lyve1 (clone ALY7, eBioscience), PE conjugated anti-Ly6C (clone HK1.4, eBioscience), PerCP-Cy5.5 conjugated anti-CD3 (clone 17A2, BioLegend), APC conjugated anti-CD206 (clone C068C2, BD Biosciences), PE-conjugated anti-FOLR2 (clone 10/FR2, BioLegend), Alexa Fluor 700 conjugated anti-CD19 (clone 6D5, BioLegend) and APC-Cy7 conjugated anti-CD11c (clone N418, BioLegend) and analyzed on a BD LSR Fortessa flow cytometer.

BMDM intracellular flow cytometry: Fixation and permeabilization were performed using a PFA/saponin based Fixation/Permeabilization kit (BD Biosciences). The cells were then stained for pro-IL-1β using a PE-Cy7 or PE-conjugated monoclonal antibody (clone NJTEN3, Life Technologies). We validated this antibody clone for this specific application using an appropriate isotype control (clone eBRG1).

Instrument

BD LSR Fortessa and BD FACSaria II

Software

FlowJo v10.8

Cell population abundance

Populations of interest were sorted to >98% purity, as measured by flow cytometric analysis of sorted populations.

Gating strategy

For all experiments, the live single cell population which formed the basis for further gating was defined based on subsequent FSC-A/SSC-A, FSC-A/FSC-H, and SSC-W/SSC-H gates. For most markers including CD45.1/2 for sorting, positive and negative gates were defined by the bimodal distribution of the fluorescence signal. For the tissue-resident macrophage flow cytometry analysis, CD206+/hi (TR) macrophages formed a separate population from CD206int (TREM2hi and inflammatory) macrophages, which was further validated by assessing its expression of CD9 (lower) and CD11c (lower), as well as FOLR2 (higher) and LYVE1 (higher), which was consistent with our scRNA-seq data.

Tick this box to confirm that a figure exemplifying the gating strategy is provided in the Supplementary Information.